NeuroImage 110 (2015) 60–77

Contents lists available at ScienceDirect

NeuroImage

journal homepage: www.elsevier.com/locate/ynimg

Influence of the head model on EEG and MEG source connectivity analyses

Jae-Hyun Cho [a,*], Johannes Vorwerk [b], Carsten H. Wolters [b], Thomas R. Knösche [a]

[a] Max Planck Institute for Human Cognitive and Brain Sciences, Leipzig, Germany
[b] Institute for Biomagnetism and Biosignal Analysis, University of Münster, Münster, Germany

ARTICLE INFO

Article history:
Accepted 23 January 2015
Available online 29 January 2015

Keywords:
EEG
MEG
Head modeling
Forward problem
Finite element model
Source reconstruction
Beamforming
Connectivity
Imaginary coherence
Generalized partial directed coherence

ABSTRACT

The results of brain connectivity analysis using reconstructed source time courses derived from EEG and MEG data depend on a number of algorithmic choices. While previous studies have investigated the influence of the choice of source estimation method or connectivity measure, the effects of the head modeling errors or simplifications have not been studied sufficiently.

In the present simulation study, we investigated the influence of particular properties of the head model on the reconstructed source time courses as well as on source connectivity analysis in EEG and MEG. Therefore, we constructed a realistic head model and applied the finite element method to solve the EEG and MEG forward problems. We considered the distinction between white and gray matter, the distinction between compact and spongy bone, the inclusion of a cerebrospinal fluid (CSF) compartment, and the reduction to a simple 3-layer model comprising only the skin, skull, and brain. Source time courses were reconstructed using a beamforming approach and the source connectivity was estimated by the imaginary coherence (ICoh) and the generalized partial directed coherence (GPDC).

Our results show that in both EEG and MEG, neglecting the white and gray matter distinction or the CSF causes considerable errors in reconstructed source time courses and connectivity analysis, while the distinction between spongy and compact bone is just of minor relevance, provided that an adequate skull conductivity value is used. Large inverse and connectivity errors are found in the same regions that show large topography errors in the forward solution. Moreover, we demonstrate that the very conservative ICoh is relatively safe from the crosstalk effects caused by imperfect head models, as opposed to the GPDC.

Introduction

While in the past the localization of brain activity was the main focus of neuroimaging, connectivity analysis is nowadays considered crucial for understanding brain function in neuroscience as well as in clinical research (Bassett and Gazzaniga, 2011; Castellanos et al., 2011; He et al., 2011; Palva and Palva, 2012; Schnitzler and Gross, 2005; Schoffelen and Gross, 2009). The notion of brain connectivity encompasses at least three major concepts: effective, functional, and structural connectivity (Friston, 1994; Horwitz, 2003). Functional and effective connectivity patterns in the human brain have been estimated from functional magnetic resonance imaging (fMRI) or from electroencephalography (EEG) and magnetoencephalography (MEG). Although the spatial resolution of EEG and MEG is lower than that of fMRI, they have high temporal resolution in the millisecond range and directly reflect neuronal activity caused by synchronous changes of membrane potentials in large numbers of neurons. For these reasons, EEG and MEG have been widely used to detect networks of neuronal activities and to estimate causality within these networks (David et al., 2006; Kamiński and Blinowska, 1991; Kiebel et al., 2006; Kus et al., 2004; Lachaux et al., 1999; Nolte et al., 2004; Rappelsberger and Petsche, 1988; Varela et al., 2001).

Functional connectivity between time courses recorded at multiple EEG and MEG sensors has been estimated using various methods, for example linear correlation in time or frequency domain (Nolte et al., 2004; Rappelsberger and Petsche, 1988) or analysis of phase synchrony (Lachaux et al., 1999; Varela et al., 2001). Likewise, directional information flow (effective connectivity) between signals has also been estimated using various methods (Baccalá and Sameshima, 2001; David et al., 2006; Granger, 1969; Kamiński and Blinowska, 1991; Kiebel et al., 2006). However, the interpretation of connectivity in sensor space is difficult because of signal mixing caused by volume conduction. Moreover, it is difficult to associate an anatomical meaning with the connections, as the measured signals do not generally locate in direct spatial proximity to the underlying sources (Castellanos et al., 2011; Palva and Palva, 2012; Schoffelen and Gross, 2009).

* Corresponding author at: Max Planck Institute for Human Cognitive and Brain Sciences, Stephanstraße 1A, 04103 Leipzig, Germany. Fax: +49 341 9940 2204.
E-mail address: jhcho@cbs.mpg.de (J.-H. Cho).

http://dx.doi.org/10.1016/j.neuroimage.2015.01.043

To overcome these drawbacks, connectivity analysis can be performed in the source space. The time courses that represent the activity of brain areas can be reconstructed by source reconstruction methods. This way, it is possible to reduce the linear mixing effect and to directly reveal the anatomical locations of interacting brain regions. Therefore, in recent years, connectivity analysis in the source space has been utilized in basic neuroscience and clinical studies (Babiloni et al., 2005; Hillebrand et al., 2012; Lu et al., 2012; Palva et al., 2010; Shim et al., 2014). However, the effect of signal mixing is not completely abolished by source reconstruction (Haufe et al., 2013; Schoffelen and Gross, 2009). Due to the non-uniqueness and ill-posedness of the neuroelectromagnetic inverse problem, spurious connections might remain, which calls for caution in the interpretation of the results. In order to ameliorate this, source reconstruction methods that suppress signal mixing (Dalal et al., 2006; Hui et al., 2010) as well as connectivity measures that attenuate the effect of signal mixing (Nolte et al., 2004) have been proposed.

To date, the accuracy of source connectivity analysis has been evaluated with respect to the employed connectivity measures and source localization methods. Astolfi et al. (2007) compared various multivariate connectivity measures derived from Granger causality, a measure for the directional information flow between time courses (Granger, 1969). They demonstrated that all the investigated methods estimated similar connectivity patterns and found that the result was mainly affected by the signal-to-noise ratio (SNR) and the signal length. To extend this study, Fasoula et al. (2013) demonstrated the different frequency resolution properties of the measures and the effect of noise variance on connectivity estimation. Sekihara et al. (2011) showed that imaginary coherence (ICoh) is far less affected by the crosstalk (or leakage) effects of the source localization method than classical coherence. In a study comparing the different source localization methods, Schoffelen and Gross (2009) pointed out that spurious correlation could occur in source connectivity analysis using the minimum-norm estimation (MNE) (Hämäläinen and Ilmoniemi, 1984, 1994) and the linearly constrained minimum variance (LCMV) beamformer (Van Veen et al., 1997), even though only uncorrelated sources were assigned. Hui et al. (2010) introduced the nulling beamformer to reduce and eliminate the crosstalk effect caused by source localization. They reported that the nulling beamformer successfully estimated the original connectivity pattern, while MNE and LCMV beamformer results contained spurious connections. Recently, Haufe et al. (2013) demonstrated that the effect of volume conduction on Granger causality based connectivity measures can be reduced using time inversion testing and that source localization methods with high spatial resolution are needed for accurate connectivity analysis in source space.

However, to the best of our knowledge, none of these studies systematically considered the influence of the head model on source connectivity analysis, in spite of the fact that forward modeling errors are known to have a significant effect on the accuracy of source analysis (Acar and Makeig, 2013; Aydin et al., 2014; Dannhauer et al., 2011; Fuchs et al., 2007; Hallez et al., 2008; Haueisen et al., 1997, 2002; Lanfer et al., 2012a,b; Montes-Restrepo et al., 2014; Stenroos et al., 2014; Wolters et al., 2006). Spherical head models (de Munck and Peters, 1993) or the boundary element method (BEM) using 3 layers for the skin, skull, and brain (Fuchs et al., 2007; Kybic et al., 2005) were used in most previous studies on source connectivity as a compromise between computational cost and accuracy.

For more accurate source analysis, it is advantageous to use a realistically shaped, sufficiently detailed and accurate head model that considers all relevant tissues. Recently, several such techniques have been proposed, including BEM with 4 or 5 tissue layers (Acar and Makeig, 2013), the finite difference method (Hallez et al., 2005; Vanrumste et al., 2000), and the finite element method (FEM) (Buchner et al., 1997; Haueisen et al., 1997; Marin et al., 1998; Schimpf et al., 2002; van den Broek et al., 1998; Wolters et al., 2004). Among these, the FEM is the most versatile, as it allows the modeling of arbitrary anisotropic conductivity profiles using any type of discretization. Although the FEM was not widely used in the past because of its large computational costs, the development of FE transfer matrix approaches (Wolters et al., 2004) has enabled high resolution FEM head modeling within acceptable computational times (Lew et al., 2009b).

With these forward solutions, previous studies showed the effect of various head model features on the accuracy of EEG/MEG forward and inverse solutions. The distinction between white and gray matter, which is usually not accounted for by conventional spherical and BEM head models, has been demonstrated to be relevant to topographic and magnitude errors in the forward solution (Haueisen et al., 1997; Ramon et al., 2004; Vorwerk et al., 2014) and to source localization errors (Acar and Makeig, 2013; Van Uitert et al., 2003). Modeling of the skull has been shown to play an important role in EEG source localization because of its low conductivity. In particular, the distinction between compact and spongy bone tissues (Dannhauer et al., 2011; Montes-Restrepo et al., 2014), the effect of skull holes and modeling simplifications (Lanfer et al., 2012b), and the role of sutures and fontanels in infants (Lew et al., 2013) have been studied. The cerebrospinal fluid (CSF) is also often neglected in conventional head modeling in spite of its high conductivity value. Wolters et al. (2006) showed that CSF highly affects the return currents of the source in the brain, and complementing studies also demonstrated strong CSF effects on both forward and inverse modeling (Acar and Makeig, 2013; Hyde et al., 2012; Lanfer et al., 2012a; Rullmann et al., 2009).

It seems likely that these effects of head model inaccuracies on source localization would also apply to source connectivity analysis from EEG and MEG data, because the source time courses are derived from the results of source localization. It is, however, not directly clear how sensitive source connectivity measures will be towards such factors. Therefore, similar studies to the ones described above should be conducted for connectivity analysis.

In the present simulation study, we jointly examined the effects of FEM head modeling on forward computation, source estimation, and, most importantly, connectivity analysis. For the simulation, a detailed and anatomically realistic head model, constructed from individual MR images and comprising distinct tissue types for white and gray matter, compact and spongy bone, as well as CSF and skin, was used as a reference model. Although this head model is also just an approximation to a real human head and there is no ultimate proof for its absolute accuracy, it represents the current state of the art of advanced head modeling. Three test head models were derived from the reference model by selectively neglecting particular features: the distinction between white and gray matter, the distinction between compact and spongy bone tissues, and the inclusion of the CSF compartment. In a fourth test model, all three simplifications were applied simultaneously, resulting in the conventional 3-layer model comprising only the skin, skull, and brain.

To investigate the differences between head models, we examined the errors in each step of the source analysis process. First, to investigate the differences between forward results, we compared the lead field matrices, which represent the interaction between sensors and source points. Second, signals of source networks were generated using neural mass modeling (Jansen and Rit, 1995), and then the LCMV beamformer was employed for source reconstruction. The LCMV beamformer has been used to reconstruct source time courses in many previous studies (Brookes et al., 2011; Hillebrand et al., 2012; Hipp et al., 2011, 2012; Kujala et al., 2007; Martino et al., 2011; Wibral et al., 2011), because its spatial resolution is higher than that of linear inverse methods if the signals are not fully correlated in time (Darvas et al., 2004; Sekihara et al., 2005). The reconstructed source time courses were assessed with regard to the ratio between reconstructed source and projected noise and to the crosstalk effects. Finally, for the source

connectivity analysis, we used the ICoh (Nolte et al., 2004) and the generalized partial directed coherence (GPDC) (Baccalá and de Medicina, 2007) as connectivity measures.

The primary objective of the present study was to examine how different aspects of head modeling affect source space connectivity analysis in EEG and MEG, and how this interacts with the location and orientation of the interacting sources. As we used very conservative connectivity measures (ICoh and GPDC), our results are expected to give insight into whether and in which regions of the brain connectivity can be reliably estimated from EEG and MEG. They will also provide answers to the question, which features of the head should be modeled in detail? We believe that this is the first systematic study on the influence of head models to the source connectivity performance using FEM as a forward procedure of the source analysis.

Methods

Head modeling

T1- and T2-weighted MR images of a healthy 25-year-old male subject were acquired on a 3T MR scanner (Magnetom Trio, Siemens, Munich, Germany) using a 32-channel head coil. For the T1-weighted MRI an MP-RAGE pulse sequence (TR/TE/TI/FA = 2300 ms/3.03 ms/1100 ms/8°, FOV = 256 × 256 × 192 mm, voxel size = 1 × 1 × 1 mm) with fat suppression and GRAPPA parallel imaging (acceleration factor = 2) was used. For the T2-weighted image an SPC pulse sequence (TR/TE = 2000 ms/307 ms, FOV = 255 × 255 × 176 mm, voxel size = 0.99 × 1.0 × 1.0 mm interpolated to 0.498 × 0.498 × 1.00 mm) was used. MR images were resampled to 1 mm isotropic resolution. The T2-weighted image was registered onto the T1-weighted images using a rigid registration approach and a cost function based on mutual information implemented in the FSL-toolbox (Smith et al., 2004).

For the construction of FEM models, different types of grids can be used. The commonly used regular hexahedral meshes allow for a fairly easy and fast model construction process and can achieve good accuracies (Rullmann et al., 2009). Tetrahedral models enable the representation of smoother and thereby more realistic tissue boundaries (Lanfer et al., 2013). This leads to a more suitable representation of the conductive head tissue compartments, which should result in an even better accuracy, however, on the cost of a more elaborate and time-consuming model generation process. Since the goal of our study is not to propose a fast model creation pipeline, but to show the effects of the modeling of the different compartments, we use the more sophisticated non-intersecting surface based constrained Delaunay tetrahedral approach, in order to rule out as much as possible effects due to insufficient model detail and numerical inaccuracies.

For the construction of the reference head model, a segmentation distinguishing the skin, compact and spongy bone, CSF, and gray and white matter was generated from the MR images. The skin and compact/spongy bone were segmented using a gray-value based active contour approach (Vese and Chan, 2002). The segmentation of the skull was then manually corrected in order to reduce skull modeling errors (Lanfer et al., 2012b; Oostenveld and Oostendorp, 2002; van den Broek et al., 1998). The foramen magnum and the two optic canals were correctly modeled as skull openings, and the segmentation was extended downwards at the neck, as recommended by Lanfer et al. (2012b). For the CSF compartment, only the superficial (subarachnoidal) CSF was modeled, while the CSF in the ventricles was ignored. This was done in order to avoid the problems of complex source space geometries under the constraint of closed and non-intersecting compartment interfaces, which are necessary for the chosen tetrahedral modeling approach (see below). Although this modeling somewhat deviates from reality, it was shown in a recent study about the influence of interior CSF by Lanfer et al. (2012a) that ignoring the interior CSF caused quite small errors to the forward and inverse solutions, except for a few very deep source positions, while ignoring the superficial CSF caused large errors. Therefore, we modeled only the superficial CSF and considered the inferior CSF as white matter in the head model. High resolution surfaces of the skin and compact and spongy bone were extracted using the software package CURRY (Compumedics Neuroscan), and a Taubin smoothing was applied to remove staircase-like effects (Taubin, 1995). The cortex surface and the surface of the white/gray matter interface were then segmented and extracted using the FreeSurfer-toolbox (Dale et al., 1999).

In order to use a constrained Delaunay tetrahedralization (CDT), all obtained surfaces were checked for intersections and those found were corrected by flattening the inner surface, guaranteeing a minimal distance between all surfaces. The CDT was executed using the software TetGen (Tetgen, 2014), and the resulting mesh consisted of 984,569 nodes and 6,107,561 elements, respectively. Fig. 1 shows an example view of the segmented head model.

Table 1 lists the conductivity values of head compartments for each head model (Akhtari et al., 2002; Baumann et al., 1997; Dannhauer et al., 2011; Fuchs et al., 2007). Four simplified test head models were derived from the reference head model (Table 1) by eliminating the distinction between gray and white matter (5C-w/g), by neglecting the distinction between compact and spongy bone (5C-c/s) and using a value of 0.01 S/m, as proposed by Dannhauer et al. (2011), by neglecting the distinction between gray matter and CSF (5C-CSF), and by applying all three simplifications at once, leading to a conventional 3-layer model (3C).

EEG and MEG sensors

We used realistic sensor configurations for EEG and MEG. The positions of 80 electrodes (10-10 system) were digitized using a Polhemus (Polhemus Inc.) device and projected onto the skin surface. For MEG, a 273-channel whole head gradiometer sensor configuration (CTF Omega 2005 MEG by MISL) was constructed.

FEM forward approach

We used the Venant direct approach to model the dipole source in the brain (Buchner et al., 1997), because of its good accuracy for sufficiently regular meshes (Lew et al., 2009b; Vorwerk et al., 2012). The FEM approach has a high computational efficiency when used in combination with the FE transfer matrix approach and with an algebraic multi grid preconditioned conjugate gradient solver (Lew et al., 2009b;

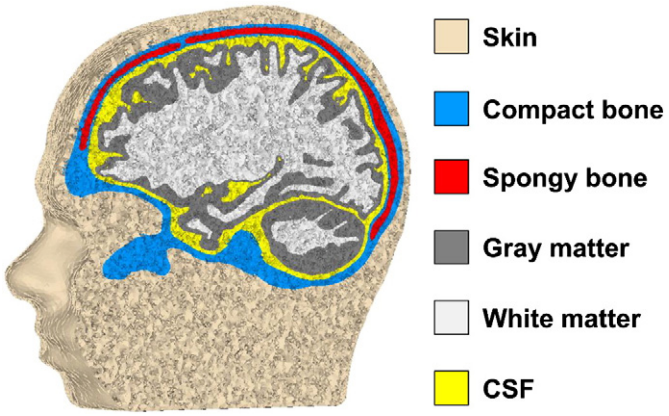

Fig. 1. Sagittal cut through the segmented reference head model comprising six tissue compartments.

Table 1
Conductivity values (unit: S/m) of the head models (*w* is the white matter, *g* is the gray matter, *c* is the compact bone, and *s* is the spongy bone).

Compartment	Reference	5C-w/g	5C-c/s	5C-CSF	3C
Brain	*w*: 0.14 *g*: 0.33	0.33	*w*: 0.14 *g*: 0.33	*w*: 0.14 *g*: 0.33	0.33
CSF	1.79	1.79	1.79	0.33	0.33
Skull	*c*: 0.0064 *s*: 0.02864	*c*: 0.0064 *s*: 0.02864	0.01	*c*: 0.0064 *s*: 0.02864	0.01
Skin	0.43	0.43	0.43	0.43	0.43

Wolters et al., 2004). All forward solutions were computed using the SimBio Toolbox (SimBio, 2014).

The time for computing the EEG and MEG transfer matrices for 80 electrodes and 273 sensors, which has to be performed only once per geometry (Wolters et al., 2004), was 666.34 s and 2294.19 s, respectively. The forward solution for each dipole then only took 0.5 ms for the EEG and 1.37 ms for the MEG. The maximum memory usage was 5.1 Gb and 8.5 Gb for EEG and MEG, respectively. These times were measured on a desktop computer (Intel Core i7-2600 @ 3.40 GHz CPU and 16 Gb RAM) running Ubuntu 11.04. The computations were performed on a single core of the CPU.

Source space

The Venant direct approach requires that the vertex closest to the source position in the head model is exclusively part of elements belonging to gray matter, the so-called Venant condition. Otherwise, modeling inaccuracies may occur, and the strength of the effects of conductivity changes in the neighboring white matter and CSF compartments might be strongly misestimated (Vorwerk, 2011). We first generated 129,640 regularly distributed source positions on the surface of the white/gray matter interface with outward surface normal directions. The source positions were then downsampled to 16,000 nodes. All vertices in the gray matter compartment fulfilling the Venant condition were computed and the source positions were moved into the direction of the next valid node, until this node became the node closest to the source position.

Forward error measures

In order to compare the forward solutions between reference and test head models, we used the relative difference measure (RDM) and the magnification factor (MAG) (Meijs et al., 1989) as

$$\mathrm{RDM}(q_i) = \left\| \frac{\mathbf{l}(q_i)}{\|\mathbf{l}(q_i)\|} - \frac{\hat{\mathbf{l}}(q_i)}{\|\hat{\mathbf{l}}(q_i)\|} \right\|, \tag{1}$$

$$\mathrm{MAG}(q_i) = \frac{\|\hat{\mathbf{l}}(q_i)\|}{\|\mathbf{l}(q_i)\|}, \tag{2}$$

where $\|\cdot\|$ represents the L_2 norm, and $\mathbf{l}(q_i)$ and $\hat{\mathbf{l}}(q_i)$ are lead field vectors of the reference head model and the test head models at location q_i, respectively (the subscript i indicates a location in source space). The RDM measures topographic difference and is bounded between 0 and 2. The MAG measures the magnitude error: 1 means no error, while deviating values indicate overestimated or underestimated magnitudes.

Source depth and orientation

In order to investigate the relationship between forward error and source position, we defined source depth and orientation. The source depth was defined as the minimal distance of the source position q_i to the inner skull surface. Fig. 2b depicts the spatial distribution of the source depth.

The source orientation was defined with respect to the radial orientation, which plays a crucial role in spherical volume conductor models for EEG, and an even greater role in MEG. In a realistic head model, spherical symmetry still plays a role, but a radial direction cannot be defined in a straightforward way anymore. Here we used the property of the vanishing magnetic field in a spherical volume conductor for a new definition. For each point in the source space the source orientation for which the MEG was minimal was defined as radial. Singular value decomposition was performed for the lead field of three orthogonal dipoles at each source position (Ahlfors et al., 2010; Huang et al., 2007; Lew et al., 2013): $[\mathbf{l}_x(q_i), \mathbf{l}_y(q_i), \mathbf{l}_z(q_i)] = \mathbf{USV}^{\mathrm{T}}$, where **U** and **V** are the left and right singular vectors, respectively, and **S** is the diagonal matrix

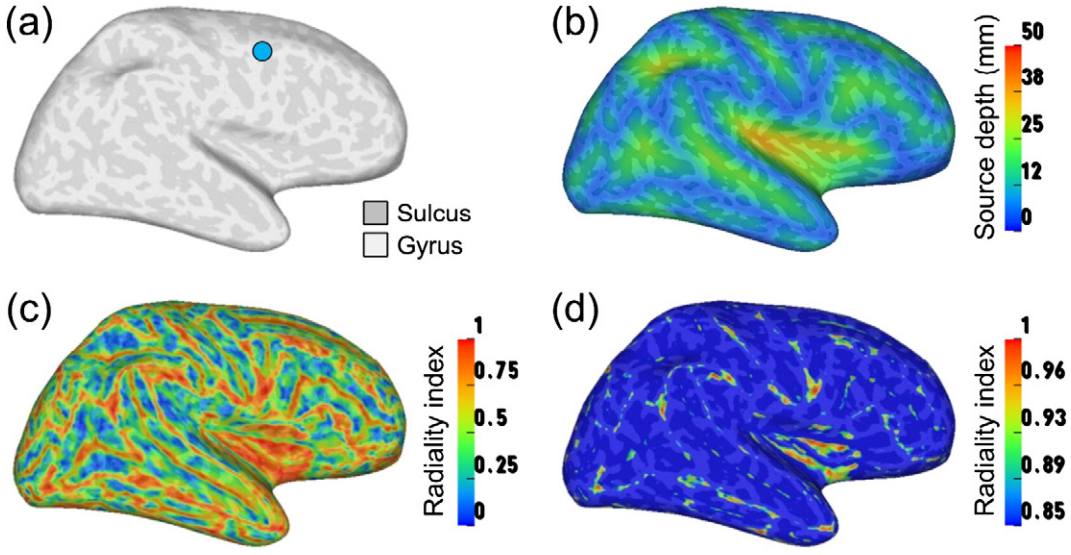

Fig. 2. (a) The inflated surface of the white/gray matter interface. The curvature of the cortex is indicated by light gray for gyri and dark gray for sulci. The blue circle represents the fixed location for source 1. (b) Distance of the sources to the inner skull surface (source depth), (c) radiality index, and (d) radiality index thresholded at 0.85, visualized on the inflated surface.

with singular values. The radial orientation was defined as the last column of **V**, corresponding to the smallest singular value in **S**. To quantify the "radiality" of the orientation of a source at a certain position on the cortex (defined by the normal direction on the cortex), the absolute cosine of the angle between normal direction and radial direction was calculated, and this value was called *radiality index*. Fig. 2c depicts the spatial distribution of the radiality index over the cortex. The normal orientation is similar to the radial orientation when the radiality index is close to 1 and it is similar to tangential orientation when the radiality index is close to 0.

LCMV beamformer

In the present study, the LCMV beamformer method (Van Veen et al., 1997) was used to reconstruct source time courses. The LCMV beamformer is an adaptive spatial filtering technique which has been widely used for source analysis because of its high spatial resolution (Sekihara et al., 2005). It is based on the assumption that the measured signals **m** at the sensors are generated by a small number N of focal neural sources $\mathbf{x}(q_r)$ at *source locations* q_r ($r = 1 \ldots N$) (the subscript r indicates source location r of the source space):

$$\mathbf{m} = \sum_{r=1}^{N} \mathbf{l}(q_r)\mathbf{x}(q_r). \tag{3}$$

The LCMV beamformer constrains a spatial filter whose output $\hat{\mathbf{x}}(q_i)$ at a particular location in the source space, called the *pointing location* q_i, is:

$$\hat{\mathbf{x}}(q_i) = \mathbf{w}^T(q_i)\mathbf{m}. \tag{4}$$

The weights of the spatial filter $\mathbf{w}(q_i)$ are selected to minimize the variance of the filter output under the constraint that signals from the pointing location are passed with a unit gain:

$$\min_{\mathbf{w}(q_i)} \mathrm{tr}\left[\mathbf{w}^T(q_i)\mathbf{C}_m\mathbf{w}(q_i)\right] \text{ subject to } \mathbf{w}^T(q_i)\mathbf{l}(q_i) = \mathbf{I}, \tag{5}$$

where $\mathbf{C}_m$ denotes the spatial covariance matrix of the measurement data. This optimization problem can be solved using Lagrange multipliers (Van Veen et al., 1997):

$$\mathbf{w}(q_i) = \mathbf{C}_m^{-1}\mathbf{l}(q_i)\left[\mathbf{l}^T(q_i)\mathbf{C}_m^{-1}\mathbf{l}(q_i)\right]^{-1}. \tag{6}$$

Connectivity measures

Multivariate autoregressive (MVAR) model

N source time courses can be represented as a vector **x**:

$$\mathbf{x}(q_r, t) = [x(q_1, t), x(q_2, t), \ldots, x(q_N, t)]^T, \tag{7}$$

where t refers to time. Then the multivariate autoregressive (MVAR) model can be expressed as:

$$\mathbf{x}(t) = \sum_{k=1}^{p} \mathbf{A}(k)\mathbf{x}(t-k) + \mathbf{E}(t), \tag{8}$$

where we omit the notation of q_r for simplicity. $\mathbf{E}(t)$ is the *N-dimensional* vector of zero-mean uncorrelated white noise, $\mathbf{A}(k)$ are the $N \times N$ matrices of model coefficients, and p is the model order. The model coefficients $\mathbf{A}(k)$ can be derived by model fitting algorithms, such as the Yule–Walker, Burg, and stepwise least squares algorithms (Kamiński and Liang, 2005; Schlögl, 2006). The model order p can be chosen by means of the logarithm of Akaike's Final Prediction Error (Akaike, 1971).

Assuming $\mathbf{A}(0) = \mathbf{I}$ and $\bar{\mathbf{A}}(k) = -\mathbf{A}(k)$ for $k > 0$, Eq. (8) can be rewritten:

$$\mathbf{E}(t) = \sum_{k=0}^{p} \bar{\mathbf{A}}(k)\mathbf{x}(t-k). \tag{9}$$

Eq. (9) can be transformed to the frequency domain by applying the Z-transform:

$$\mathbf{E}(f) = \bar{\mathbf{A}}(f)\mathbf{X}(f), \tag{10}$$

where

$$\bar{\mathbf{A}}(f) = \sum_{k=0}^{p} \bar{\mathbf{A}}(k)\exp(-2\pi i k f \Delta t) \tag{11}$$

with $i^2 = -1$ and Δt is the data sampling interval.

Imaginary coherence (ICoh)

From the estimated model coefficients, the estimated spectral density matrix $\mathbf{S}(f)$ of the dataset is given by

$$\mathbf{S}(f) = \mathbf{X}(f)\mathbf{X}^*(f) = \bar{\mathbf{A}}^{-1}(f)\mathbf{E}(f)\left(\bar{\mathbf{A}}(f)^{-1}\mathbf{E}(f)\right)^*, \tag{12}$$

where * represents the matrix transpose and complex conjugate operation. The ICoh (Nolte et al., 2004) can be derived as

$$\mathrm{ICoh}_{ij}(f) = \frac{\mathrm{Im}\left(S_{ij}(f)\right)}{\sqrt{S_{ii}(f)S_{jj}(f)}}, \tag{13}$$

where $\mathrm{Im}(\cdot)$ indicates the imaginary part and $S_{ij}(f)$ is an element of $\mathbf{S}(f)$. The ICoh excludes coherent sources with zero time lag and therefore reduces the effect of field spread and crosstalk. The ICoh ranges between -1 and 1. If the value of ICoh is positive, then source time courses i and j are interacting and source time course j is earlier than i, indicating that information is flowing from j to i.

Generalized partial directed coherence (GPDC)

The partial directed coherence (PDC) (Baccalá and Sameshima, 2001) is defined using the MVAR model coefficient as

$$\mathrm{PDC}_{ij}(f) = \frac{\bar{A}_{ij}(f)}{\sqrt{\sum_{k=1}^{N}|\bar{A}_{kj}(f)|^2}}, \tag{14}$$

where $\bar{A}_{ij}(f)$ is an element of $\bar{\mathbf{A}}(f)$. The PDC denotes the ratio between flow from signal j to signal i and sum of flows from signal j to all other signals. N is the number of signals. The magnitude-squared PDC is generally used and it ranges between 0 and 1. A PDC value close to 1 indicates that signal i is caused by signal j, and a PDC value close to 0 means a lack of such a relation.

The results of the PDC could be distorted by very different noise variances in the source time courses (Baccalá and de Medicina, 2007; Fasoula et al., 2013). In order to reduce this effect, the generalized PDC (GPDC) was introduced (Baccalá and de Medicina, 2007). It is defined as

$$\mathrm{GPDC}_{ij}(f) = \frac{\frac{1}{C_{ii}}\bar{A}_{ij}(f)}{\sqrt{\sum_{k=1}^{N}\frac{1}{C_{kk}^2}\left|\bar{A}_{kj}(f)\right|^2}}, \tag{15}$$

where C_{ii} is the i-th diagonal element of the noise covariance matrix $\mathbf{C} = \mathbf{E}(f)\mathbf{E}(f)^*$. The magnitude-squared GPDC is typically used and it ranges between 0 and 1.

Simulation signal

In order to investigate the effect of the head model on source connectivity analysis, we assume a two-source scenario with a simple source connectivity model generating two source time courses. The location of one source is kept fixed (blue circle in Fig. 2a), while the other source is positioned at all remaining locations of the source space. We selected the location of source 1 such that it has small RDM and radiality index in order to reduce the effect of the head modeling errors caused by source 1 (source depth about 9.67 mm, radiality index about 0.02, RDM values for EEG: 5C-w/g ≈ 0.066, 5C-c/s ≈ 0.023, 5C-CSF ≈ 0.073, and 5C ≈ 0.067, and RDM values for MEG: 5C-w/g ≈ 0.075, 5C-c/s ≈ 0.007, 5C-CSF ≈ 0.081, and 5C ≈ 0.089).

A neural mass model (David et al., 2005; Jansen and Rit, 1995) was used to generate source time courses for two unidirectionally coupled sources. In this model, oscillations emerge from the interaction between pyramidal neurons with excitatory and inhibitory interneurons (Spiegler et al., 2010). To generate two source time courses with information flow from source 1 to 2, two local circuits, each comprising three masses of interneurons and pyramidal neurons, were connected such that the output of the pyramidal neurons in source 1 was connected to the input of the excitatory interneurons in source 2. The parameters of the populations were chosen according to the study of David et al. (2005). The simulated signals were sampled at 200 Hz, resulting in 4,000 sample points. The EEG and MEG signals were then generated by multiplying the simulated source time courses with the lead field matrix of the reference head model and adding white Gaussian noise.

For the two-source scenario, the covariance matrix is expressed as

$$\mathbf{C}_m = \sigma_0^2\mathbf{I} + \sigma_{r1}^2\mathbf{l}(q_{r1})\mathbf{l}(q_{r1})^T + \sigma_{r2}^2\mathbf{l}(q_{r2})\mathbf{l}(q_{r2})^T, \tag{16}$$

where σ_0^2 is the noise variance, and σ_{r1}^2 and σ_{r2}^2 are the powers of the sources r1 and r2, respectively. q_{r1} and q_{r2} are the source locations. The measure of the strength of the r-th source can be defined as

$$\frac{\sigma_r^2\left\|\mathbf{l}(q_r)^2\right\|}{\sigma_0^2}. \tag{17}$$

This is often called input SNR (Sekihara and Nagarajan, 2008; Sekihara et al., 2005). In the two-source scenario, the total input SNR was used to represent the ratio between the total strength of the two sources and the noise variance:

$$\frac{\sigma_{r1}^2\left\|\mathbf{l}(q_{r1})^2\right\| + \sigma_{r2}^2\left\|\mathbf{l}(q_{r2})^2\right\|}{\sigma_0^2}. \tag{18}$$

The input SNR is the number of sensors times larger than the conventionally used SNR. For example, the input SNR is equal to 300 when the SNR for the 80-channel EEG is about 3.75 and the SNR for the 273-channel MEG is about 1.1.

Evaluation of source reconstruction

The quality of the source connectivity analysis relies on the performance of the source reconstruction method. Increasing projected noise in the source space and crosstalk effects of other sources are likely to affect the source connectivity estimation. Therefore, we first calculated the ratio between reconstructed source power and projected noise power. Second, we estimated in a two-source scenario how much the reconstruction of one of the sources is contaminated by crosstalk from the other source. Then, in order to assess the amount of spurious connectivity caused by the crosstalk, we measured the correlation between the beamformer weights (vector **w** from Eq. (6)) of the two sources.

Output SNR of the LCMV beamformer

In source space we calculated a ratio between reconstructed source power and projected noise power to compare the properties of the spatial filters obtained from the reference head model and test head models. This ratio is customarily called the output SNR (or Z^2) and it can be expressed as (Sekihara et al., 2004)

$$Z^2(q_i) = \frac{\mathbf{w}^T(q_i)\mathbf{C}_m\mathbf{w}(q_i)}{\mathbf{w}^T(q_i)\sigma_0^2\mathbf{I}\mathbf{w}(q_i)}. \tag{19}$$

As the reconstructed source power includes the projected noise power, the Z^2 value can be interpreted as 1 plus original source power divided by projected noise ratio. In other studies, this value was also called the pseudo-Z (Vrba and Robinson, 2001) or the neural activity index (Van Veen et al., 1997).

Crosstalk to signal ratio

In order to evaluate the crosstalk to signal ratio of the spatial filters for the head models, we used the beam response analysis, which expresses the sensitivity of a point source in one location to a source at another location (Sekihara and Nagarajan, 2008). The beam response, $R(q_i, q_r)$, is defined as

$$\hat{\mathbf{x}}(q_i) = \mathbf{w}^T(q_i)\mathbf{m} = \sum_{r=1}^{N}\mathbf{w}^T(q_i)\mathbf{l}(q_r)\mathbf{x}(q_r) = \sum_{r=1}^{N}R(q_i, q_r)\mathbf{x}(q_r) \tag{20}$$

(as mentioned above, the subscript i indicates a pointing location of the beamformer and the subscript r indicates the actual location of a focal source). In the present simulation, we assumed a two-source scenario in which the source locations were already known as q_{r1} and q_{r2}. The beam response at the two locations can then be expressed as

$$\begin{bmatrix}\hat{x}(q_{r1})\\ \hat{x}(q_{r2})\end{bmatrix} = \begin{bmatrix}R(q_{r1}, q_{r1}) & R(q_{r1}, q_{r2})\\ R(q_{r2}, q_{r1}) & R(q_{r2}, q_{r2})\end{bmatrix}\begin{bmatrix}x(q_{r1})\\ x(q_{r2})\end{bmatrix}. \tag{21}$$

The main diagonal elements $R(q_{r1}, q_{r1})$ and $R(q_{r2}, q_{r2})$ are magnitude factors, while the off-diagonal elements define the crosstalk. The crosstalk to signal ratio (CSR) can be expressed as

$$\mathrm{CSR}(q_{r1}) = \frac{R(q_{r1}, q_{r2})}{R(q_{r1}, q_{r1})} \quad \text{and} \quad \mathrm{CSR}(q_{r2}) = \frac{R(q_{r2}, q_{r1})}{R(q_{r2}, q_{r2})}. \tag{22}$$

Weight correlation

While CSR represents the crosstalk effect in each source time course, the crosstalk effect caused by both of the two source time courses could be assessed by examining the correlation between weights calculated by the LCMV beamformer (vector **w** from Eq. (6)), the so-called weight correlation (Brookes et al., 2011). The weight correlation was computed using the correlation coefficient between weights of the LCMV beamformer at source 1 and source 2. If the weights are highly correlated, the reconstructed signals can also be correlated and this may appear as crosstalk effect in the LCMV beamformer based source connectivity analysis.

Evaluation of the measured source connectivity

The autoregressive model underlying the computation of the connectivity measures was estimated using the ARFIT-toolbox (Schneider and Neumaier, 2001), and the SIFT-toolbox (Delorme et al., 2011) was used to compute ICoh and GPDC. These computations were performed using the software MATLAB (MathWorks).

Furthermore, a relative error (Astolfi et al., 2007) was computed to compare the connectivity results between reconstructed source time courses and original source time courses obtained by ICoh and GPDC.

The relative error RE_{ij} of the connectivity from signal j to signal i is defined as

$$RE_{ij} = \frac{\sqrt{\left(\overline{\mu}_{ij}(f_1,f_2) - \overline{\mu}_{ij,ori}(f_1,f_2)\right)^2}}{\sqrt{\left(\overline{\mu}_{21,ori}(f_1,f_2)\right)^2}}, \quad (23)$$

where $\overline{\mu}_{ij}(f_1,f_2)$ is the mean value of the causality measure (ICoh or GPDC) from signal j to signal i over the frequency range from f_1 to f_2 for reconstructed source time courses, and $\overline{\mu}_{ij,ori}(f_1,f_2)$ is the mean value of the causality measure for the original source time courses in the same frequency range. The absolute error (the numerator in the equation of the relative error) was normalized to $\overline{\mu}_{21,ori}(f_1,f_2)$ in order to assess the relative change between the absolute error and the connectivity result of the original signals for the direction of the causal interaction.

For the ICoh, we only considered the direction from source 1 to 2 since the results for the opposite direction are just the reverse. In contrast, for the GPDC we considered both directions because the GPDC can measure bidirectional relationships. Note that the direction from source 2 to 1 refers to a spurious connection since we only modeled causal flow from source 1 to 2 in the simulation setting. The main frequency band of the source time courses generated by the neural mass model was from 3 to 7 Hz, so this frequency band was used to calculate the relative error.

Visualization

For visual inspection, the results in source space were mapped onto the inflated surface of the interface between white and gray matter, which comprised 129,707 nodes and 259,482 elements. Fig. 2a depicts the inflated surface, where light gray marks gyri and dark gray sulci. The underlying curvature is visualized through the semi-transparent color map (see, e.g., Fig. 2b). All visualizations were carried out using the software SCIRun (SCIRun, 2014).

Results

Forward simulations

The spatial distributions for RDM and MAG were mapped onto the inflated surface of the white/gray matter interface (Fig. 3). The dependence of the forward error on radiality index and source depth is shown in heat maps (Fig. 4). While the spatial distribution maps in Fig. 3 show only the more superficial parts (source depth < 30 mm) of the right hemisphere, the heat maps represent the entire source space. Contour lines on the heat map represent the number of samples per bin, thus indicating the reliability of the map (see Fig. 5 for quantitative values). The two local peaks in the contour lines indicate roughly the crests of gyri (radiality index > 0.75 and source depth < 5 mm) and the sulcal walls (radiality index < 0.4 and 5 mm < source depth < 15 mm), respectively.

5C-w/g model

For EEG, large RDM errors (>0.2) are mainly found along the crests of gyri (source depths < 5 mm and radiality index > 0.6) as well as for very deep sources. The magnitude is slightly overestimated in some superficial areas (crests of gyri; source depth < 5 mm and radiality index > 0.95) and in the insula, and slightly underestimated in some sulcal regions. For MEG, large RDM errors (>0.2) are observed mainly in areas with high radiality (>0.95) (i.e., the crests of gyri and the troughs of sulci), irrespective of the source depth, as well as in very deep areas. The magnitude is overestimated in sulcal walls and slightly overestimated at gyral crests. The patchiness of the RDM maps (Fig. 3), especially in the MEG case, is due to undersampling of the cortical curvature by the source space — only some dipoles exactly hit the gyral/sulcal line and already a small deviance causes a large difference in radiality. The same patchiness can be observed in the spatial distribution of the radiality index in Fig. 2d.

5C-c/s model

In the EEG case, RDM and MAG spatial and heat maps show that the negligence of the compact/spongy bone distinction clearly has

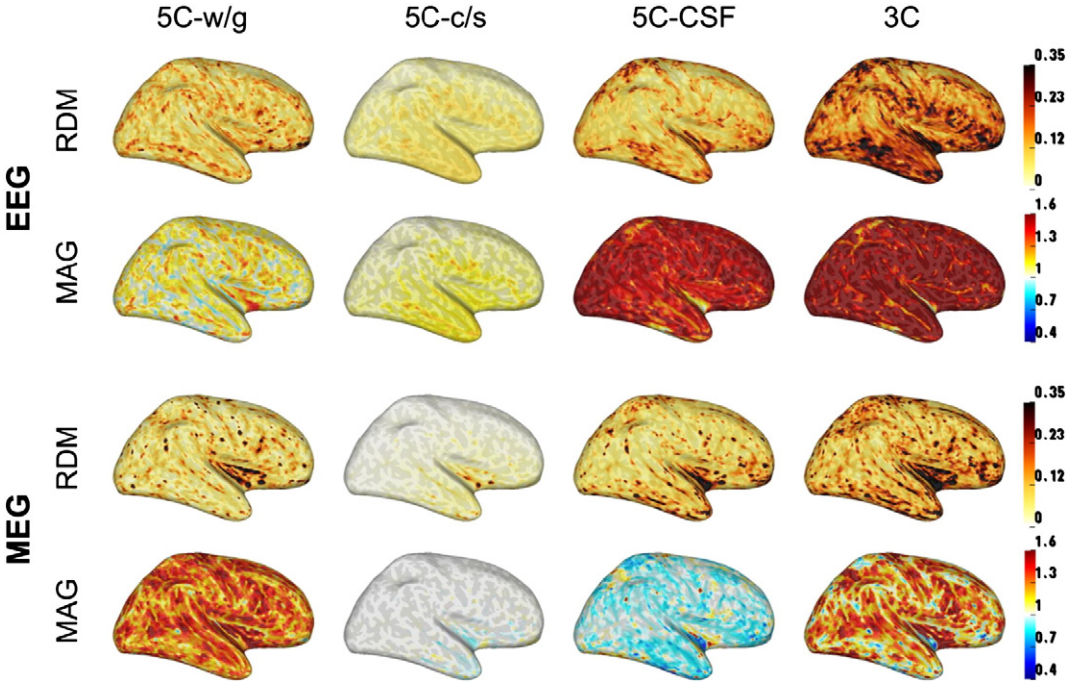

Fig. 3. RDM and MAG for the test head models in EEG and MEG plotted on the inflated surface of the white/gray matter interface.

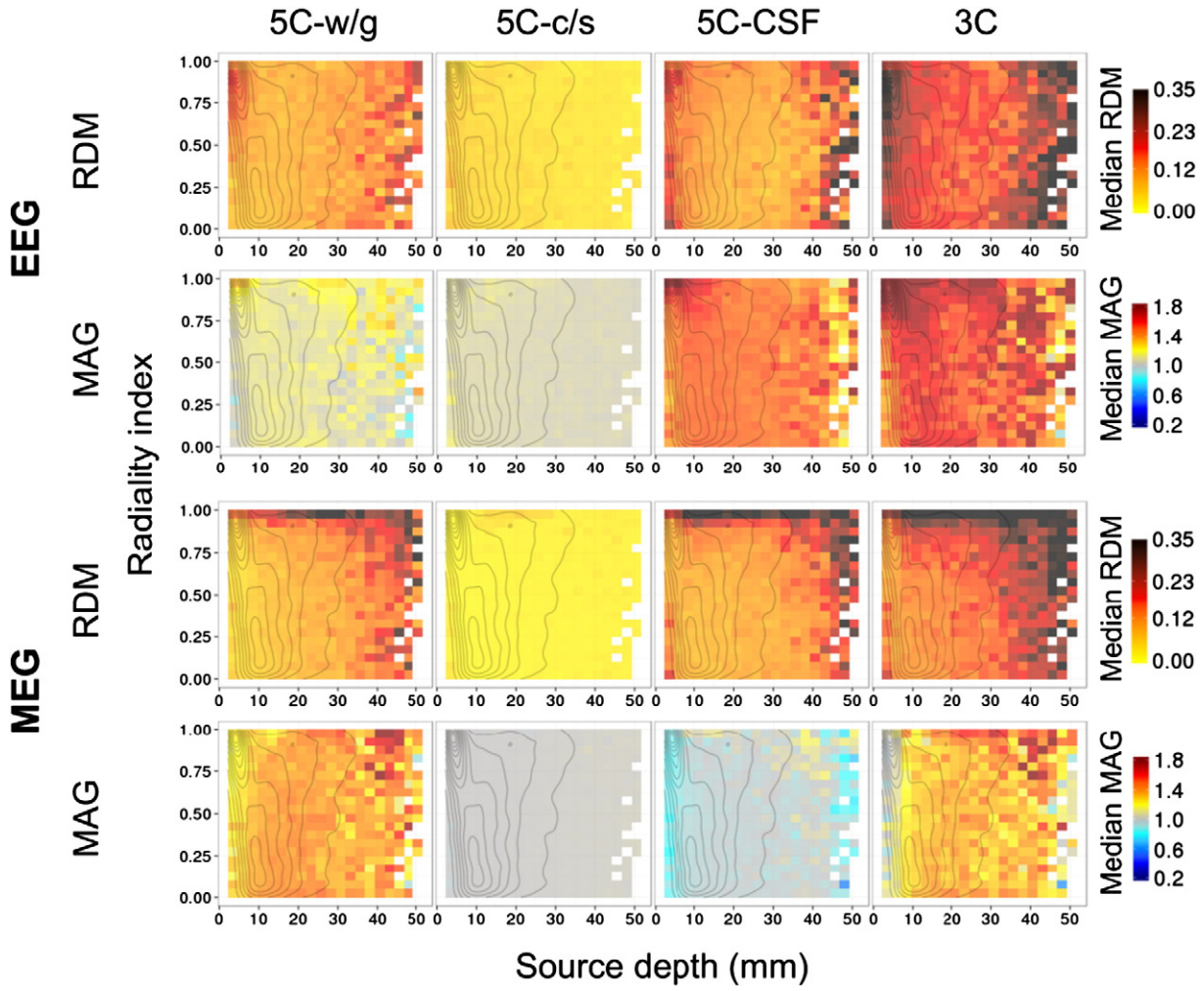

Fig. 4. Heat maps for RDM and MAG against source depth and radiality index in EEG and MEG. The plotted values are the medians per bin (bin width 5% of maximum, i.e., 0.05 for radiality index and 2.6 mm for source depth). The contour lines indicate the sample count per bin (see Fig. 5 for interpretation). White colored bins contain no samples.

a relatively small impact on the forward solution compared to the other investigated simplifications, provided that an optimized skull conductivity value is used. In temporal areas, RDM and MAG are somewhat increased, although the errors are smaller than for the other test models. This can be explained by the fact that the skull in the temporal areas is almost entirely composed of compact bone, and the optimized skull conductivity value, 0.01 S/m, is slightly larger than the conductivity value for the compact bone, 0.0064 S/m. The spatial distribution of the RDM error mapped onto the non-inflated white matter surface with spongy bone boundaries is shown in Fig. 6. The areas underneath the spongy bone show small RDM, while the RDM error is larger in temporal areas and at the top of the parietal lobe (note that Figs. 3 and 6 use different color bar ranges). The RDM error at the top of the parietal lobe is not clearly visible in Fig. 3 because of the view angle. As expected, not modeling the compact and spongy bone distinction had nearly no effect on both RDM and MAG for MEG. Only a weak influence at the insula and temporal pole was found.

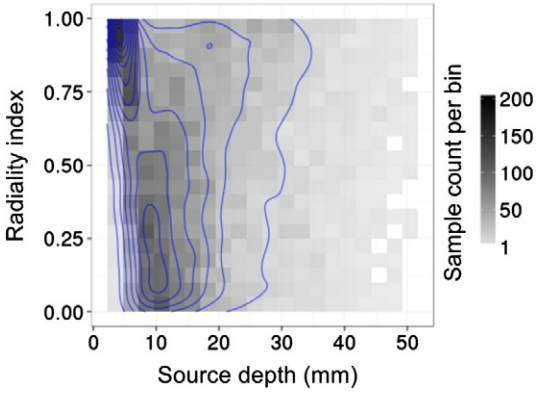

Fig. 5. Heat map and corresponding contour lines for the sample count per bin as a function of source depth and radiality index.

5C-CSF

Neglecting the CSF causes RDM errors in approximately the same areas as for neglecting the white/gray matter distinction (for EEG they are slightly stronger and less dependent upon the radiality index). In contrast, the MAG errors are, while also following the same spatial patterns, much stronger. In particular, neglecting the CSF leads to a magnitude overestimation for EEG and an underestimation for MEG.

3C model

The errors for the simple 3C model are largely a superposition of the errors occurring with the other test model, in particular 5C-w/g and 5C-CSF. In some cases the errors even compensate each other, e.g., the MAG error in superficial regions for MEG.

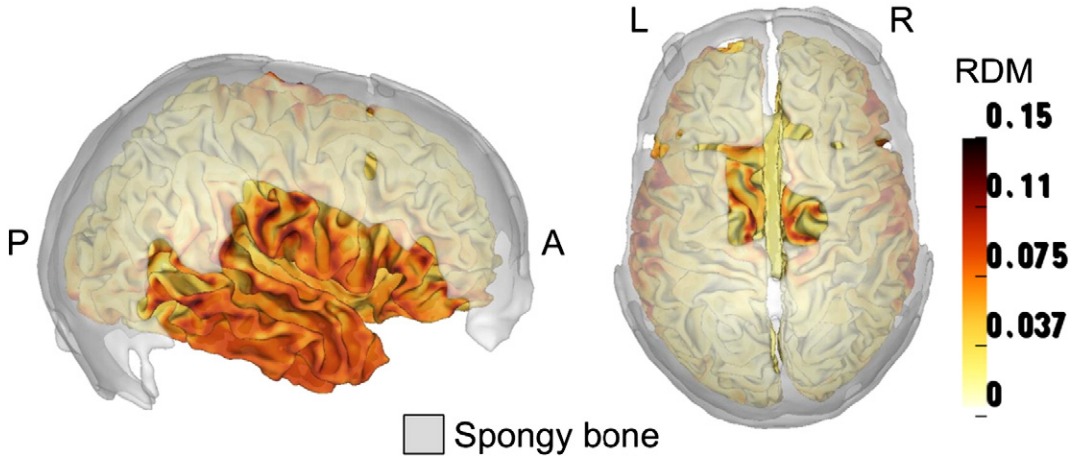

Fig. 6. RDM for the 3C-c/s head model visualized on the non-inflated surface of the white/gray matter interface with the spongy bone boundary overlaid (transparent gray color). Obviously, the RDM error is larger in parts of the brain not covered by spongy bone. However, this error is still smaller than those of the other test head models (see Fig. 3). Note that, although in principle spongy bone also exists in temporal areas, its layer is very thin there and could therefore not be captured by the resolution of our FEM model.

Source reconstruction

As explained in the Method section, we investigated the properties of the spatial filters of the LCMV beamformer with respect to head model simplifications on the example of the source reconstruction in a two-source scenario using three different measures: output SNR, CSR, and weight correlation.

Output SNR (Z^2)

The ratio between reconstructed source power and projected noise power was assessed using the output SNR (Z^2) in the two-source scenario. A small Z^2 value means that the reconstructed source contains a large amount of noise. We computed $\ln(Z^2)$ for each head model and different input SNRs (1 and from 20 to 500 in increments of 20). Here, ln denotes the natural logarithm. As the Z^2 value is always greater than one, $\ln(Z^2)$ is larger than zero. The computed $\ln(Z^2)$ values were then sorted in ascending order of the associated RDM. We plotted the heat maps for the reference head model using the mean output SNR value at each input SNR, because naturally there was no RDM value for the reference head model. The results for source 1 and source 2 are plotted as heat maps in Fig. 7. To investigate the spatial distribution of $\ln(Z^2)$, we plotted maps for each head model for an input SNR of 300 (Fig. 8) as an example. In the spatial distribution maps for source 1, the output SNR value for source 1 is mapped to the corresponding location of source 2 (while source 1 is fixed in one location).

In general, at extremely small input, SNR (input SNR = 1) $\ln(Z^2)$ is small, and then rises sharply if the input SNR is increased only slightly (Fig. 7). Further increase of the input SNR often causes $\ln(Z^2)$ to decay again. For source 1, the slope of this decay does not depend on the RDM (accuracy of the forward solution) for EEG, and only slightly so for MEG (it becomes steeper for larger RDM). For the reference and the 5C-c/s models, $\ln(Z^2)$ does not decrease at all with increasing input SNR. This relative insensitivity to the RDM (i.e., the forward error) is easily explained by the fact that the position of source 1 (fixed source) was chosen such that the RDM is small for all test models. The spatial maps (Fig. 8) reveal that for source 1 deeper areas show smaller $\ln(Z^2)$ in EEG, while the crests of gyri and troughs of sulci show smaller $\ln(Z^2)$ in MEG. The $\ln(Z^2)$ values are large (>2) near the fixed point (i.e., when both sources are very close to each other), but these patterns are different between EEG and MEG. This could be due to the different crosstalk effects of the test head models.

In contrast, for source 2 the maximum $\ln(Z^2)$ decreases and the slope of its decay with increasing input SNR increases if the RDM is increased (except for the reference model of course). Hence, for any given input SNR, $\ln(Z^2)$ decreases with increasing RDM, which is also reflected by the observation that the spatial maps (Fig. 8) very much resemble the spatial maps of the RDM (Fig. 3). The effect is least pronounced for the 5C-c/s model (for MEG even absent). In general, the $\ln(Z^2)$ values were smallest for the 3C model, followed by the 5C-CSF, 5C-w/g, and 5C-c/s models.

Crosstalk to signal ratio (CSR)

We quantify the extra crosstalk between two sources introduced by the particular head model simplifications embodied in the test models. In Fig. 9, the CSR was plotted on the inflated surface for an input SNR of 300. Note that CSR values close to +1 or −1 indicate large crosstalk and values close to 0 low crosstalk.

In the reference model the CSR maps for both source 1 and source 2 show similar patterns. Noticeable CSR values are found near the location of source 1, i.e., for cases where both sources are located very close to each other. Due to source orientation similarity between source 1 (fixed on sulcal wall) and source 2, large CSR values are generally found in the sulcal walls (with different signs depending on their mutual parallel or antiparallel orientation). Furthermore, large CSR values are found more widely spread over the entire cortex in EEG as compared to MEG, where they are more concentrated to some vicinity of source 1. This difference could be caused by the different numbers of sensors (MEG has 273 coils, while EEG has 80 electrodes).

The CSR maps for the 5C-c/s model are quite similar to those of the reference model except for source 2 with EEG. In that case, somewhat larger CSR values are found near the position of source 1 and in temporal areas, similar to the RDM error for the 5C-c/s case (Fig. 3).

For the other test head models, large CSR values can be found in widespread areas and near the position of source 1 (fixed source). For source 1, while the patterns of the CSR maps for EEG and MEG are different in detail, large CSR values are found mainly in sulcal walls. For source 2, the pattern of the CSR map is different to that of source 1, and larger CSR values are found in a wider area for EEG than for MEG, especially in the temporal and insular cortex, although the distribution patterns are slightly different.

The box plots in Fig. 10 show the dependence of the CSR value on the input SNR. In the reference model, the CSR slightly decreases with increasing input SNR, since spatial resolution of the LCMV beamformer increases with SNR (Brookes et al., 2008; Sekihara et al., 2005). However, in most test head models (except 5C-c/s), the CSR does not depend on the input SNR. This finding indicates that most large CSR values in the test head models are not caused

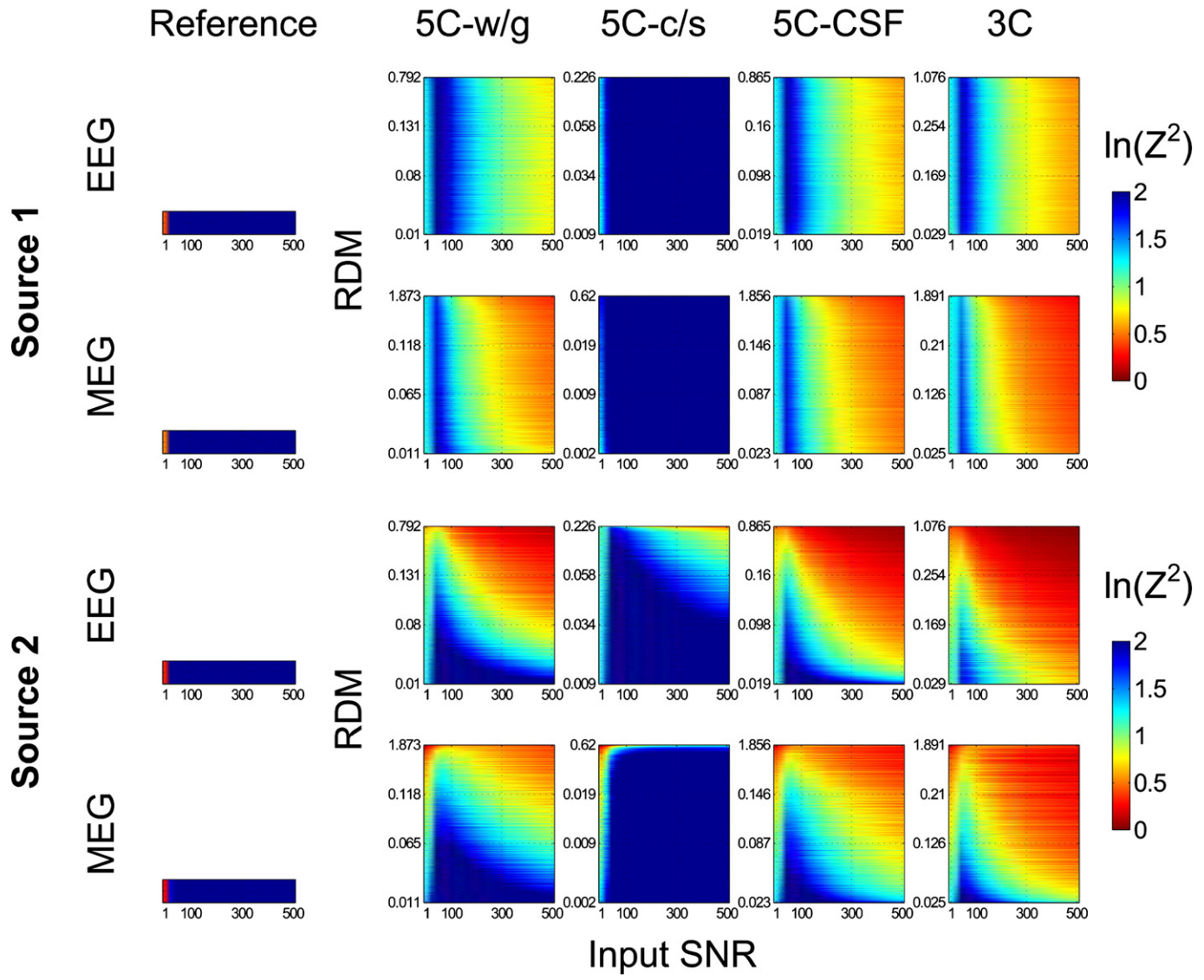

Fig. 7. Heat map of $\ln(Z^2)$ of sources 1 and 2, as function of input SNR and RDM in EEG and MEG. Note the different RDM ranges of the y-axis. The output SNR was calculated with different input SNRs. Then, the output SNR was ordered in ascending order of the RDM value for each head model. The heat maps for the reference head model represent the mean output SNR value at each input SNR.

by the decreased spatial resolution of the LCMV beamformer, but by the head modeling errors.

Weight correlation

To investigate crosstalk effects caused by both of the two sources, the weight correlation between source 1 and source 2 was calculated and mapped onto the location of source 2 on the inflated surface (Fig. 11). While the CSR represents crosstalk effects in each source, the weight correlation represents crosstalk effects in each pair of two sources.

In the reference model, large weight correlation values were found in almost all places, mainly in the sulcal walls (Fig. 11), while large CSR values were mainly found near the position of fixed source 1 (i.e., when the distance between source 1 and source 2 is small) (Fig. 9). The large weight correlation values for MEG are found more in the vicinity of the position of source 1 than for EEG in the reference model case, which could be due to the different numbers of sensors, similar to the CSR results (Fig. 9).

In the other test head models, large weight correlation values were found in widespread areas with different patterns for both EEG and MEG (Fig. 11). These patterns were not similar to the CSR maps (Fig. 9). In 5C-c/s model and 3C model for EEG, although widespread areas exhibited large weight correlations, the values were smaller than for other head models.

In order to investigate the effect of different input SNRs, the weight correlations were computed using different input SNRs (100, 200, 300, 400, and 500). See box plots in Fig. 12. It turned out that the input SNR does not strongly influence the weight correlation. However, unlike in the CSR case (Fig. 10), the weight correlation values of the reference model are quite large and similar to those of the test head models. Moreover, the weight correlation value of the 3C model for EEG is smaller than those of the other head models.

Source connectivity analysis

To investigate the effects of the simplified head models on the source connectivity analysis, we calculated the relative error of ICoh and GPDC between the original and reconstructed source time courses in the frequency range from 3 to 7 Hz. We considered the connectivity flow from source 1 to 2 (1→2) for both measures. However, the connectivity

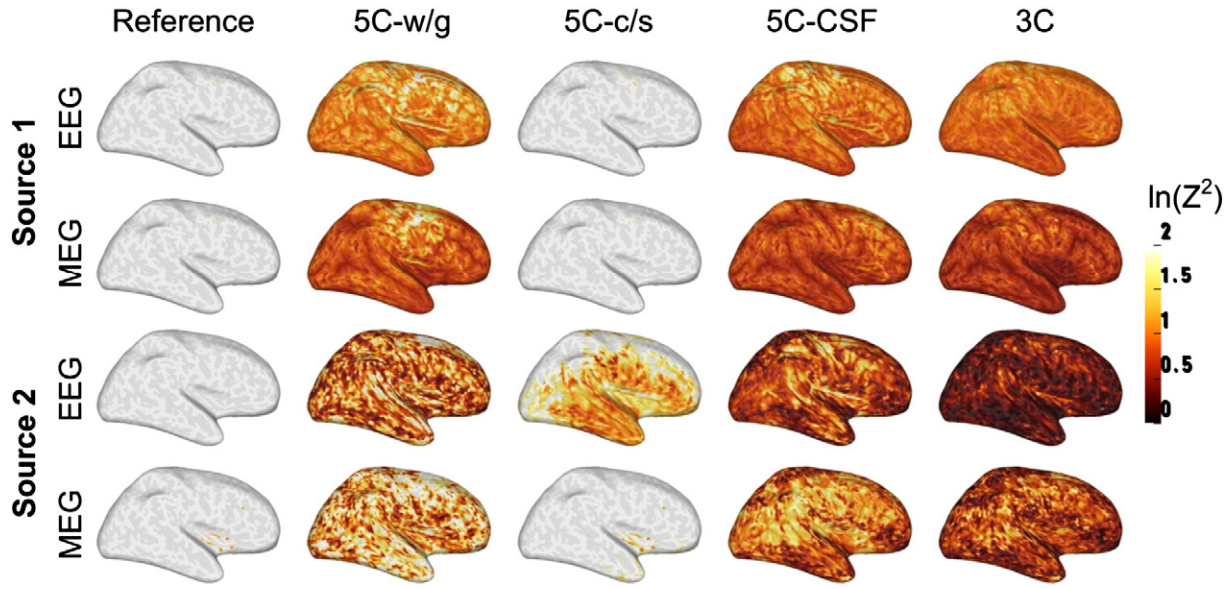

Fig. 8. $\ln(Z^2)$ for sources 1 and 2 in EEG and MEG with input SNR of 300, plotted on the inflated white/gray matter interface. Note that in the maps for source 1, the $\ln(Z^2)$ value for source 1 is mapped onto the corresponding location of source 2 for visualization purposes because the location of source 1 is fixed in one location and only the location of source 2 varies.

flow from source 2 to 1 (2→1) was only considered for GPDC, because the lCoh is a unidirectional measure (the result for the opposite direction is just the reverse). The spatial distribution maps of the relative errors for an input SNR of 300 are shown in Fig. 13. As obtained by the logarithm of Akaike's Finite Prediction Error, the MVAR model order was 10 for the original source time courses and 9.21 ± 2.01 (mean ± standard deviation) for the reconstructed source time courses.

Reference model

When using the same model for simulation and reconstruction, the relative errors in both lCoh and GPDC were very low everywhere (even lower for lCoh). So, in principle, it is possible to reconstruct the connectivity from EEG and MEG data. However, some spurious connections are found near the position of source 1 (i.e., if variable source 2 is located near fixed source 1) in GPDC for source 2→1. Since we only modeled causal flow for source 1→2 in the simulation setting, GPDC value for source 2→1 indicates spurious connectivity. Although the weight correlation map in Fig. 11 revealed large correlation values in widespread areas, the spatial distribution patterns of the relative error in connectivity are very similar to the CSR maps for the reference model (Fig. 9).

5C-w/g model

Relative error maps of lCoh and GPDC for source 1→2 show a very similar distribution pattern for RDM (Fig. 3) and output SNR for source 2 (Fig. 8). For lCoh the relative errors are quite small in most positions (even lower for MEG) and larger errors occur only at very few locations. In contrast, the relative errors for the GPDC are somewhat larger and more widespread. This could be due to the crosstalk effect. In the GPDC source 2→1 case, large relative errors are found in wide areas in both EEG and MEG, and the distribution pattern is similar to the one for weight correlations (Fig. 11).

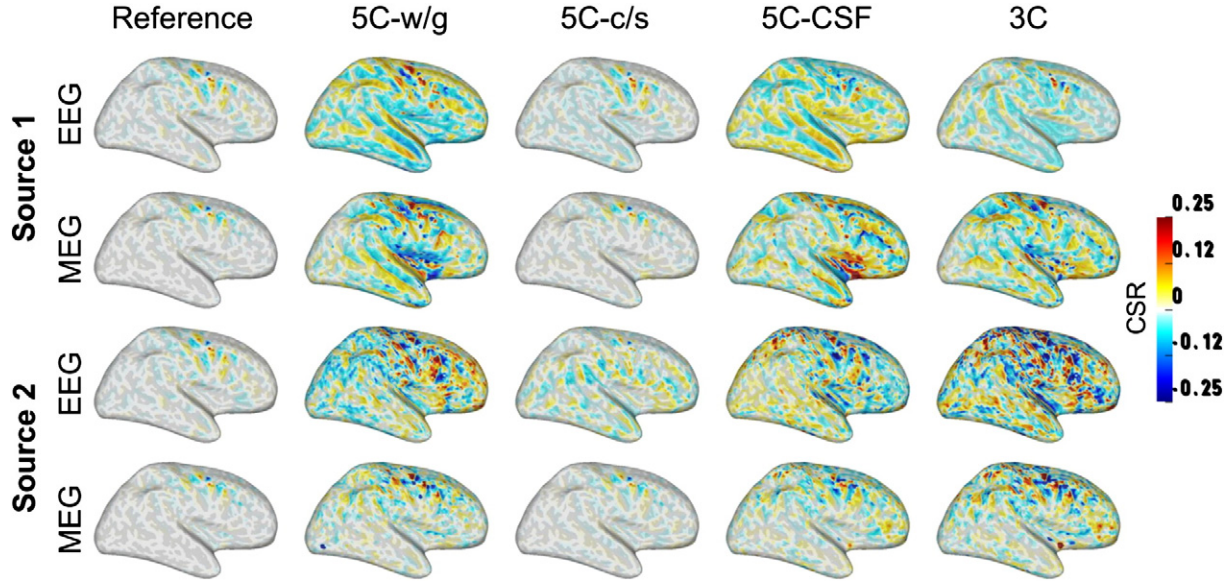

Fig. 9. Crosstalk to signal ratio (CSR) for sources 1 and 2 in EEG and MEG with an input SNR of 300. CSR values close to 0 indicate small crosstalk. Note that in the maps for source 1, the CSR for source 1 is mapped onto the corresponding location of source 2 for visualization purpose because the location of source 1 is fixed in one location and only the location of source 2 varies.

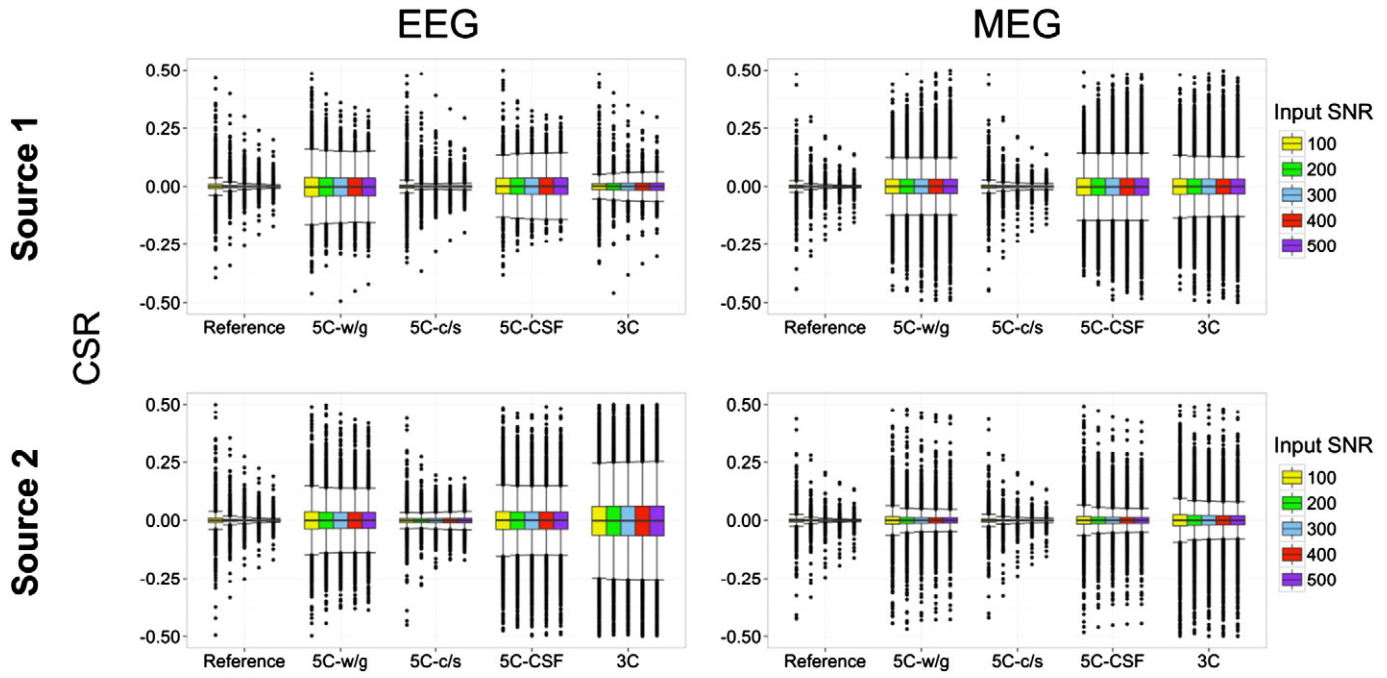

Fig. 10. Box plots for crosstalk to signal ratio (CSR) in EEG and MEG computed with different input SNRs. The middle, bottom, and top of each rectangular box represent the median, 25th percentile, and 75th percentile, respectively. The whiskers extend 1.5 times the interquartile range between the 25th and 75th percentiles. The black dots represent the outliers.

5C-c/s model

Although weight correlation values in some areas were large (Fig. 11), results for both ICoh and GPDC show low relative connectivity errors, similar to the reference model. Only the spurious connectivity for source 2→1 estimated with GPDC from EEG is more widespread.

5C-CSF model

Leaving out the CSF compartment from the head model produces, for both EEG and MEG, strong relative errors mostly in both superficial and deep positions, but not so much in intermediate positions (where the source orientations are more tangential). Again, the spatial pattern is similar to the RDM (Fig. 3) and the output SNR (Fig. 8) maps and the relative errors for GPDC are much stronger and widespread than the ones for ICoh. In GPDC for the source 2→1 case, large relative errors are found with a similar spatial pattern in the weight correlation (Fig. 11).

3C model

In this model, which constitutes a combination of the simplifications of the other three test models, the error in the estimation of the true connectivity from source 1→2 is a combination of the errors in the other models, with a slight superadditivity in the EEG case. In contrast, for the spurious connectivity 2→1, the errors seem to reduce with respect to the single violations in 5C-w/g and 5C-CSF, indicating that the effects of both simplifications partly cancel each other.

Box plots in Fig. 14 show the relative error for ICoh and GPDC as a function of the input SNR (100, 200, 300, 400, and 500). In the ICoh and GPDC source 1→2 cases, the relative errors increase for both EEG and MEG with increasing input SNR, except for the reference and 5C-c/s models. This finding might be related to the output SNR value because the output SNR of the LCMV beamformer is decreased in certain regions in which head modeling errors (RDM) are large. On the other hand, the relative errors in GPDC for source 2→1 are not noticeably changed in spite of the increased input SNR, except for the reference and 5C-c/s models. Since source 1 was fixed in a location with low RDM, the relative errors for source 2→1 are mainly affected by the crosstalk effect caused by the imperfect head modeling rather than the change of the input SNR.

Discussion

One key question in head modeling is which types of tissue to consider. Here we investigated three additions to the classical 3-layer head model that have been currently discussed: the distinction between white and gray matter in the brain (Acar and Makeig, 2013; Güllmar

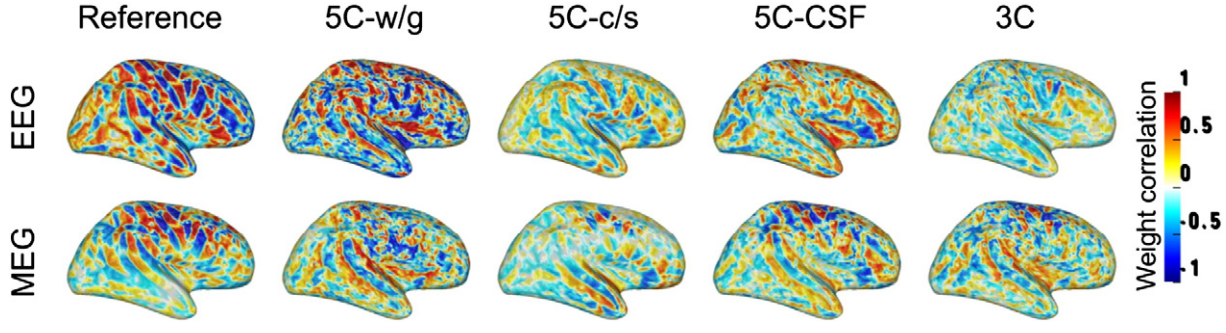

Fig. 11. Weight correlation of the LCMV beamformer between sources 1 and 2 with input SNR 300.

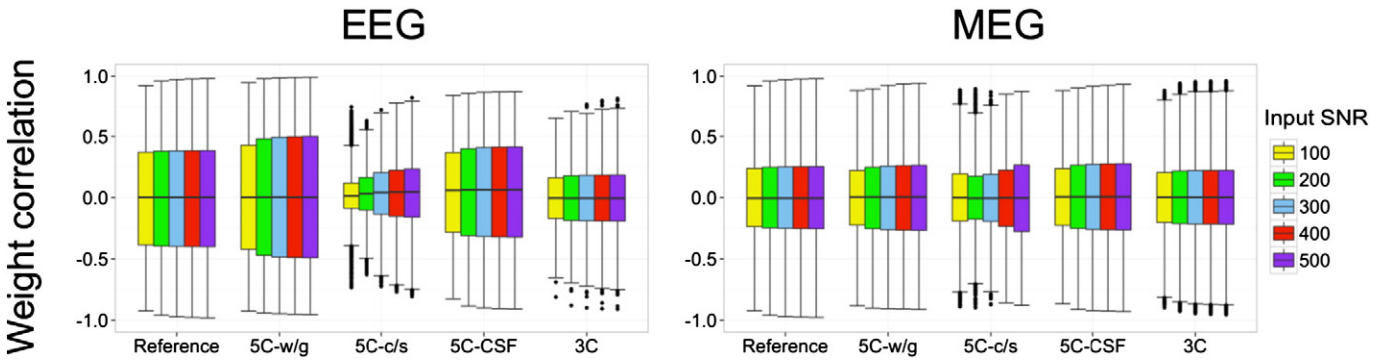

Fig. 12. Box plots for weight correlation of the LCMV beamformer between sources 1 and 2 in EEG and MEG, computed with different input SNRs. For further information about the box plot, see the caption of Fig. 10.

et al., 2010; Ramon et al., 2004; Vorwerk et al., 2014), the distinction between compact and spongy bone in the skull (Dannhauer et al., 2011; Montes-Restrepo et al., 2014; Ramon et al., 2004; Sadleir and Argibay, 2007; Vorwerk et al., 2014), and the inclusion of a CSF compartment (Acar and Makeig, 2013; Lanfer et al., 2012a; Ramon et al., 2004; Vorwerk et al., 2014; Wolters et al., 2006). Besides the effect of these features in forward and inverse analyses of EEG and MEG, we also investigated how important they are for source connectivity analysis. As inverse procedure, we employed an LCMV beamformer, which has the reputation of high spatial resolution in certain scenarios (Sekihara et al., 2005) and is especially suited for the reconstruction of uncorrelated focal (dipolar) sources. To assess the connectivity, we used ICoh and GPDC; especially the first of which has a reputation for largely suppressing spurious connectivity arising from volume conduction effects (Nolte et al., 2004).

Effects of the head compartments

The CSF compartment

The CSF compartment is disregarded in the conventionally used 3-layer head model. However, our results show that the exclusion of the CSF compartment has considerable influence, not only on forward modeling and source reconstruction (as shown before by, e.g., Vorwerk et al., 2014; Acar and Makeig, 2013; Hyde et al., 2012; Lanfer et al., 2012a; Rullmann et al., 2009), but also on the source

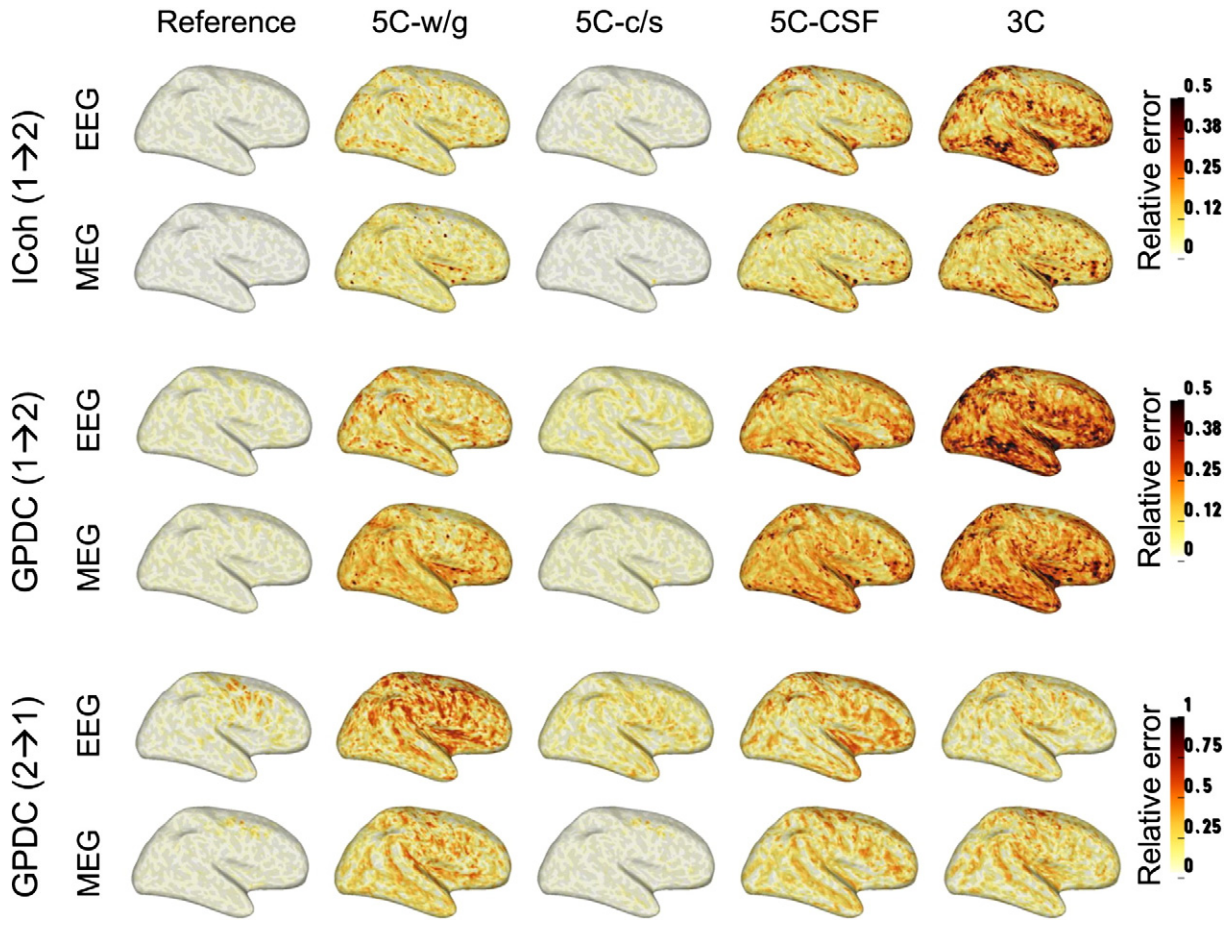

Fig. 13. The relative error between the ICoh and GPDC results (3–7 Hz) of the original simulation time courses and those of reconstructed time courses in EEG and MEG when the input SNR is 300. 1→2 indicates the information flow from source 1 to 2, and 2→1 indicates the information flow from source 2 to 1.

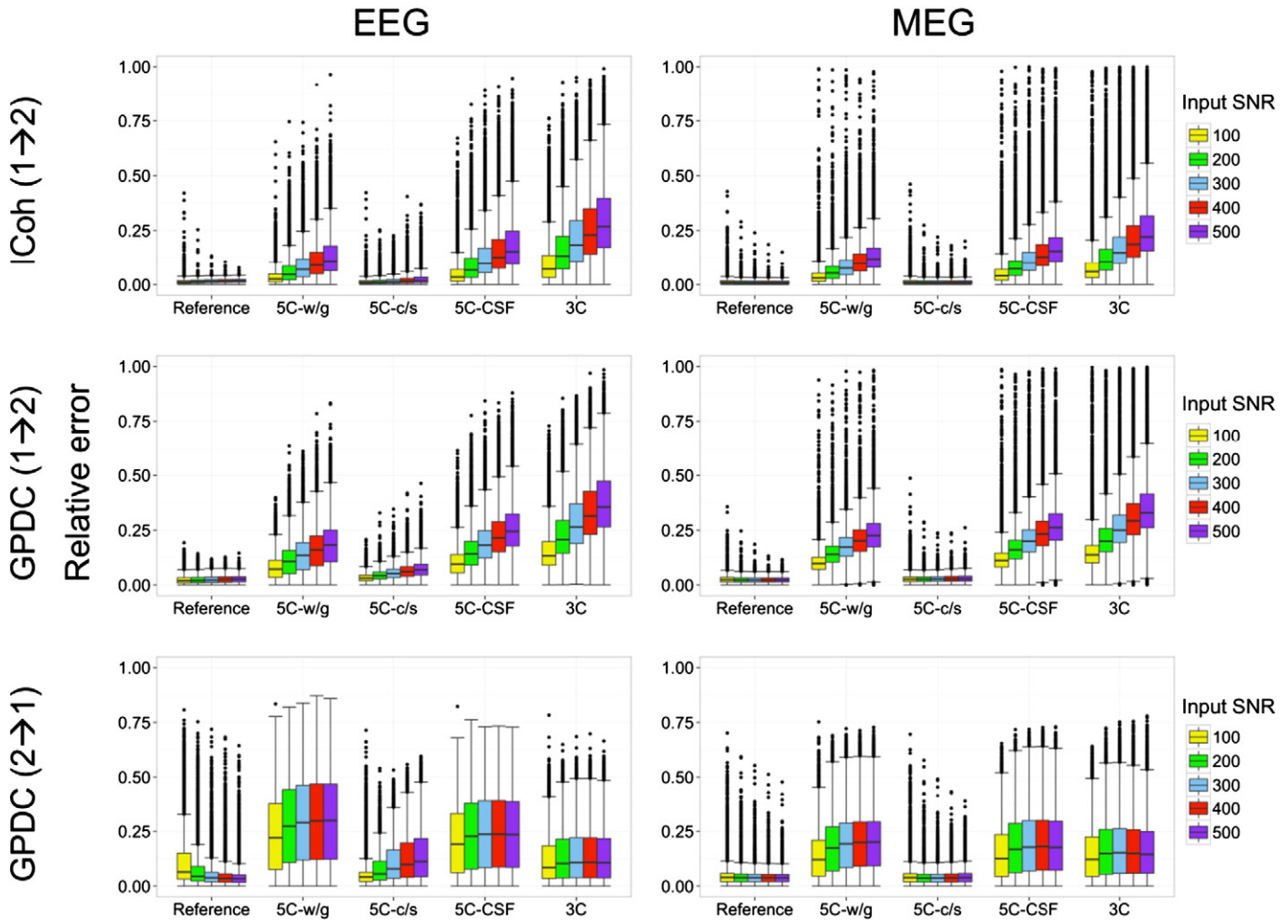

Fig. 14. Box plots for relative error between the ICoh and GPDC results (3–7 Hz) of the original simulation time courses and those of reconstructed time courses computed with different input SNRs. For further information of the box plot, see the caption of Fig. 10.

connectivity analysis for both EEG and MEG. Large errors in connectivity estimates were found in the same areas where large topographic errors in the forward solution occurred. These errors were considerably larger than for the other investigated head model simplifications and therefore dominated the error pattern of the 3C model. Moreover, the error in the GPDC estimate was directly affected by the crosstalk effect caused by not considering the high conductivity value of the CSF compartment. This finding is in line with previous studies on the effect of the CSF compartment in source analysis. They demonstrated that ignoring the CSF causes distortions in estimated current flow (Wolters et al., 2006), EEG potentials (Ramon et al., 2004), and dipole source localization (Acar and Makeig, 2013; Lanfer et al., 2012a; Wolters et al., 2006). In EEG experiments, Rice et al. (2013) showed that changing the subject's position from prone to supine had a significant effect on the EEG signal magnitudes, because of changes in the CSF layer thickness. Furthermore, a forward simulation study on head modeling by Vorwerk et al. (2014) showed that ignoring CSF has a large influence on the signal topography in both EEG and MEG, especially for superficial areas. Hence, the CSF compartment seems to be the most important addition to the classical 3-shell head model from both the source localization and connectivity analysis points of view.

Distinction between white and gray matter

The distinction between white and gray matter also has not been considered in most of the previous studies on source analysis. Here, we found that neglecting this distinction causes a decrease in output SNR in such regions that also showed large topographic errors in the forward solution. This in turn affected the results of the source connectivity analysis. Moreover, crosstalk effects caused by the head modeling error also affected the results obtained by GPDC. These findings are in accordance with previous source analysis studies. They showed that removing the white/gray matter distinction caused topography and magnitude error for both EEG and MEG (Vorwerk et al., 2014), decreased scalp potential for EEG (Ramon et al., 2004), and forward and inverse error for MEG (Van Uitert et al., 2003).

Distinction between compact and spongy bone

Ignoring the compact/spongy bone distinction showed, as expected, almost no effect on MEG and a relatively weak effect on EEG. Although some small errors in the EEG forward solution occurred near the temporal lobe and near the top of the head (see Figs. 3 and 6) as shown by Vorwerk et al. (2014), these errors did not have a large influence on the results of the inverse and connectivity analysis. The small errors in the forward solution might reflect some mismatch between the optimal skull conductivity and the local skull structure, which in the temporal regions contains very little spongy bone. In summary, our results together with previous findings confirm that it is sufficient in most cases to model the skull as a homogeneous compartment with an appropriate ("optimal") conductivity. This value has been shown to be critical by Dannhauer et al. (2011) and was estimated in that paper to be about 0.01 S/m. In order to further increase accuracy, one

could use calibrating methods to determine the effective skull conductivity (Aydin et al., 2014; Huang et al., 2007; Lew et al., 2009a). Besides the skull conductivity, also the geometry of the skull is important. For example, Lanfer et al. (2012b) showed that various errors and simplifications, in particular the common practice of simplifying the complicated skull base and to cut off models directly underneath the brain, can cause intolerable errors in forward computation and source localization.

For the MEG case, we found only very small effects of the way the skull is modeled onto forward, inverse, and connectivity analysis. This is in agreement with common belief and most previous studies (Hämäläinen et al., 1993). On the other hand, a recent study by Stenroos et al. (2014) came to the conclusion that skull modeling can also be important for MEG.

Effects of source orientation

In our simulations, we assumed that the sources were represented by point dipoles with surface normal orientation. Most of the larger errors for EEG were found in superficial areas, while source orientation had no influence. In contrast, large errors for MEG were found in regions where the radiality index was over 0.95. By definition these were the source orientations with the smallest MEG signal (i.e., the lowest SNR). Hence, MEG-based connectivity analysis should be complemented by a computation of the radiality indices of the involved sources, and discarded if these values are too high. It is relatively simple to compute a radiality map for any individual brain (see, e.g., Fig. 2d).

Effects of head modeling errors on LCMV beamformer

We found that source analysis using the LCMV beamformer on EEG or MEG was affected by the head modeling errors, leading to decreased output SNR and increased crosstalk. The output SNR inversely correlated with the topographic errors in the forward solution (RDM) as well as with the input SNR. These findings are in agreement with the results of Steinsträter et al. (2010), who studied anisotropy of the skull conductivity in EEG source analysis.

In the reference head model, although large weight correlation values were found in widespread areas (Fig. 11), noticeable CSR and relative errors for GPDC were only found when sources 1 and 2 were quite near to each other. However, large CSR values in the test head models were found in widespread areas and did not noticeably change even though the input SNR was increased. The crosstalk effect caused by head modeling errors was paralleled by the similarly distributed relative GPDC error and large weight correlation. This implies that crosstalk caused by head model errors can affect the source connectivity analysis even though the source positions are quite distant from each other.

Effects of head modeling errors on connectivity measures

The ICoh method was designed to be less affected by volume conduction (Nolte et al., 2004). In a source connectivity study by Sekihara et al. (2011), the ICoh performed better than classical coherence in source space connectivity analysis, because it was less affected by the crosstalk effect of the inverse algorithm, provided that its spatial resolution was high enough. Likewise, our results showed that ICoh was less influenced by the crosstalk effect caused by head modeling errors, as compared to the GPDC method. However, large relative errors for ICoh were found in some regions and the relative error maps were very similar to the RDM and output SNR (inversely) maps. It could be inferred, therefore, that the results obtained by ICoh are also affected by imperfect head modeling, albeit less severely.

The results of GPDC from source 1 to 2 were affected by decreased output SNR as well as by the crosstalk effect. On the other hand, in GPDC from source 2 to 1 (representing spurious connectivity, as there was no causal interaction in the original signals), mainly the crosstalk affected the results of GPDC and the error patterns were very similar to the large weight correlation. This finding implies that the errors in GPDC could occur due to the highly correlated weights of the LCMV beamformer caused by head modeling errors, and that weight correlation between source locations should be checked before source connectivity analysis.

The crosstalk effect caused by the LCMV beamformer in the results of partial directed coherence (PDC), the method upon which GPDC is based, has been studied by Hui et al. (2010). To reduce this effect, they applied a nulling beamformer (or suppression beamformer (Dalal et al., 2006)), which is a modified version of the LCMV beamformer, where a spatial filter is obtained by nulling other source signals from specific locations in source space. They demonstrated that the nulling beamformer could reduce the crosstalk effect caused by the inverse algorithm in the results of PDC. However, they did not consider the influence of the head modeling error on the source connectivity analysis. The effects of the head modeling errors are likely to remain even if the nulling beamformer method is applied. This is demonstrated by the ICoh results (Fig. 13), where, despite the removal of almost all the crosstalk, the error in connectivity largely remains.

While the results of ICoh were generally better than those of GPDC in the two-source scenario with a simple connectivity pattern (ICoh has the advantage of being less affected by crosstalk), one should be aware that ICoh could cause additional errors in multivariate cases. The ICoh is able to measure bivariate unidirectional causal flow, while the GPDC is able to measure multivariate uni- and bidirectional causal flow. Bivariate methods can evaluate the interactions by considering pairs of signals, but this could cause some spurious connections since it does not distinguish between direct and indirect connections (Blinowska, 2011; Kus et al., 2004).

Limitations and future study

Although the reference head model is anatomically more plausible than the conventionally used 3-layer or spherical head models, it is also a simplification of the reality. Therefore, it is important to note that the results of the present simulation study are subject to the assumption that the reference head model is a reasonable approximation to the real human head.

In our simulation, the white matter was simplified using an isotropic conductivity value in the reference head model. However, the white matter has anisotropic conductivity with higher conductivity along fibers and lower conductivity perpendicular to fibers. Previous studies reported that the white matter anisotropy caused return currents along the white matter fibers (Wolters et al., 2006) and affected the localization of sources near the white matter (Güllmar et al., 2010; Hallez et al., 2008; Haueisen et al., 2002). The head modeling study by Vorwerk et al. (2014) also demonstrated that topography errors were found in some regions in the crests of gyri and the troughs of sulci when the white matter anisotropy was not considered, although the errors were much smaller than the effect of ignoring the white and gray matter distinction or the CSF. Based on the present simulation results, we would expect that some errors in source connectivity analysis might occur in these regions. Future work should therefore include the white matter anisotropy to investigate its effect on source connectivity analysis.

In order to assume a practical relevance, we used realistic sensor configurations for the EEG and MEG. Although the results in CSR and weight correlation maps appear to show effects of the different sensor numbers (MEG being more focal than EEG, especially in the reference head model), our results about the effect of head modeling errors are not likely to be highly influenced by the different sensor numbers.

Note that, unlike for the test head model cases, we used the same lead field matrix in both forward and inverse procedures for the reference head model case. This is actually an unrealistic case, and thus the

simulation results for the reference head model were almost perfect (this is the so-called inverse crime (Kaipio and Somersalo, 2007)). Although the reference head model case is impractical, it helps us to separate errors coming from the head modeling error from those coming from the inverse procedure (e.g., the results about crosstalk effect in our simulation).

Our study is, of course, limited by the fact that we did not exhaustively study all possible inverse algorithms and connectivity measures. Instead, we used a source localization method that was designed for high spatial selectivity and two connectivity measures that are known for suppressing spurious connectivity. Here, the main focus was the head model. A systematic comparison of inverse algorithms and connectivity measures will have to be done in a future study.

Conclusions

To investigate the influence of the head model, we compared the reference head model and the test head models, thereby assuming that the reference model is an appropriate approximation to the real human head. Our results show that the head modeling errors caused by neglecting particular head compartments affect source reconstruction as well as connectivity analysis in both EEG and MEG. The distinction between white and gray matter and the inclusion of the CSF compartment have not usually been considered in head modeling for source analysis, but are shown to be important for source connectivity analysis in both EEG and MEG. The distinction between compact and spongy skull proved to be less critical to the source connectivity analysis in EEG, when an optimal skull conductivity value was used, and virtually unimportant for MEG. When using MEG to estimate sources and source connectivity, a radiality check should be performed and areas with large radiality indices should not be considered. Furthermore, it was found that source reconstruction and source connectivity errors spatially coincided with topographical forward errors (RDM), which strengthens the relevance of forward simulation studies (e.g., Vorwerk et al., 2014). Finally, the very conservative ICoh proved to be much safer to use with imperfect head models than the GPDC. As in our results the crosstalk errors of the GPDC looked similar to the spatial distribution pattern of the large weight correlation, the weight correlation should be carefully checked when using the LCMV beamformer for connectivity analysis.

Acknowledgment

This research was supported by the German Research Foundation (DFG) through projects KN588/4-1 and WO1425/2-1, 3-1 and the priority program SPP1665 (project WO1425/5-1).

References

Acar, Z.A., Makeig, S., 2013. Effects of forward model errors on EEG source localization. Brain Topogr. 26, 378–396. http://dx.doi.org/10.1007/s10548-012-0274-6.

Ahlfors, S.P., Han, J., Belliveau, J.W., Hämäläinen, M.S., 2010. Sensitivity of MEG and EEG to source orientation. Brain Topogr. 23, 227–232. http://dx.doi.org/10.1007/s10548-010-0154-x.

Akaike, H., 1971. Autoregressive model fitting for control. Ann. Inst. Stat. Math. 23, 163–180. http://dx.doi.org/10.1007/BF02479221.

Akhtari, M., Bryant, H.C., Mamelak, a.N., Flynn, E.R., Heller, L., Shih, J.J., Mandelkern, M., Matlachov, A., Ranken, D.M., Best, E.D., DiMauro, M.A., Lee, R.R., Sutherling, W.W., 2002. Conductivities of three-layer live human skull. Brain Topogr. 14, 151–167. http://dx.doi.org/10.1023/A:1014590923185.

Astolfi, L., Cincotti, F., Mattia, D., Marciani, M.G., Baccala, L.A., De Vico Fallani, F., Salinari, S., Ursino, M., Zavaglia, M., Ding, L., Edgar, J.C., Miller, G.A., He, B., Babiloni, F., 2007. Comparison of different cortical connectivity estimators for high-resolution EEG recordings. Hum. Brain Mapp. 28, 143–157. http://dx.doi.org/10.1002/hbm.20263.

Aydin, Ü., Vorwerk, J., Küpper, P., Heers, M., Kugel, H., Galka, A., Hamid, L., Wellmer, J., Kellinghaus, C., Rampp, S., Wolters, C.H., 2014. Combining EEG and MEG for the reconstruction of epileptic activity using a calibrated realistic volume conductor model. PLoS One 9, e93154. http://dx.doi.org/10.1371/journal.pone.0093154.t006.

Babiloni, F., Cincotti, F., Babiloni, C., Carducci, F., Mattia, D., Astolfi, L., Basilisco, A., Rossini, P.M., Ding, L., Ni, Y., Cheng, J., Christine, K., Sweeney, J., He, B., 2005. Estimation of the cortical functional connectivity with the multimodal integration of high-resolution EEG and fMRI data by directed transfer function. NeuroImage 24 (1), 118–131. http://dx.doi.org/10.1016/j.neuroimage.2004.09.036.

Baccalá, L.A., de Medicina, F., 2007. Generalized partial directed coherence. Digital Signal Processing, 2007 15th International Conference on. IEEE, pp. 163–166 http://dx.doi.org/10.1109/ICDSP.2007.4288544.

Baccalá, L.A., Sameshima, K., 2001. Partial directed coherence: a new concept in neural structure determination. Biol. Cybern. 84, 463–474. http://dx.doi.org/10.1007/PL00007990.

Bassett, D.S., Gazzaniga, M.S., 2011. Understanding complexity in the human brain. Trends Cogn. Sci. 15, 200–209. http://dx.doi.org/10.1016/j.tics.2011.03.006.

Baumann, S.B., Wozny, D.R., Kelly, S.K., Meno, F.M., 1997. The electrical conductivity of human cerebrospinal fluid at body temperature. IEEE Trans. Biomed. Eng. 44, 220–223. http://dx.doi.org/10.1109/10.554770.

Blinowska, K.J., 2011. Review of the methods of determination of directed connectivity from multichannel data. Med. Biol. Eng. Comput. 49, 521–529. http://dx.doi.org/10.1007/s11517-011-0739-x.

Brookes, M.J., Vrba, J., Robinson, S.E., Stevenson, C.M., Peters, A.M., Barnes, G.R., Hillebrand, A., Morris, P.G., 2008. Optimising experimental design for MEG beamformer imaging. NeuroImage 39, 1788–1802. http://dx.doi.org/10.1016/j.neuroimage.2007.09.050.

Brookes, M.J., Hale, J.R., Zumer, J.M., Stevenson, C.M., Francis, S.T., Barnes, G.R., Owen, J.P., Morris, P.G., Nagarajan, S.S., 2011. Measuring functional connectivity using MEG: methodology and comparison with fcMRI. NeuroImage 56, 1082–1104. http://dx.doi.org/10.1016/j.neuroimage.2011.02.054.

Buchner, H., Knoll, G., Fuchs, M., Rienäcker, A., Beckmann, R., Wagner, M., Silny, J., Pesch, J., 1997. Inverse localization of electric dipole current sources in finite element models of the human head. Electroencephalogr. Clin. Neurophysiol. 102, 267–278. http://dx.doi.org/10.1016/S0013-4694(96)95698-9.

Castellanos, N.P., Bajo, R., Cuesta, P., Villacorta-Atienza, J.A., Paúl, N., Garcia-Prieto, J., Del-Pozo, F., Maestú, F., 2011. Alteration and reorganization of functional networks: a new perspective in brain injury study. Front. Hum. Neurosci. 5, 1–13. http://dx.doi.org/10.3389/fnhum.2011.00090.

Dalal, S.S., Sekihara, K., Nagarajan, S.S., 2006. Modified beamformers for coherent source region suppression. IEEE Trans. Biomed. Eng. 53, 1357–1363. http://dx.doi.org/10.1109/TBME.2006.873752.

Dale, A.M., Fischl, B., Sereno, M.I., 1999. Cortical surface-based analysis: I. Segmentation and surface reconstruction. NeuroImage 9, 179–194. http://dx.doi.org/10.1006/nimg.1998.0395.

Dannhauer, M., Lanfer, B., Wolters, C.H., Knösche, T.R., 2011. Modeling of the human skull in EEG source analysis. Hum. Brain Mapp. 32, 1383–1399. http://dx.doi.org/10.1002/hbm.21114.

Darvas, F., Pantazis, D., Kucukaltun-Yildirim, E., Leahy, R.M., 2004. Mapping human brain function with MEG and EEG: methods and validation. NeuroImage 23 (Suppl. 1), S289–S299. http://dx.doi.org/10.1016/j.neuroimage.2004.07.014.

David, O., Harrison, L., Friston, K.J., 2005. Modelling event-related responses in the brain. NeuroImage 25, 756–770. http://dx.doi.org/10.1016/j.neuroimage.2004.12.030.

David, O., Kiebel, S.J., Harrison, L.M., Mattout, J., Kilner, J.M., Friston, K.J., 2006. Dynamic causal modeling of evoked responses in EEG and MEG. NeuroImage 30, 1255–1272. http://dx.doi.org/10.1016/j.neuroimage.2005.10.045.

de Munck, J.C., Peters, M.J., 1993. A fast method to compute the potential in the multisphere model. IEEE Trans. Biomed. Eng. 40, 1166–1174. http://dx.doi.org/10.1109/10.245635.

Delorme, A., Mullen, T., Kothe, C., Akalin Acar, Z., Bigdely-Shamlo, N., Vankov, A., Makeig, S., 2011. EEGLAB, SIFT, NFT, BCILAB, and ERICA: new tools for advanced EEG processing. Comput. Intell. Neurosci. 2011, 1–12. http://dx.doi.org/10.1155/2011/130714.

Fasoula, A., Attal, Y., Schwartz, D., 2013. Comparative performance evaluation of data-driven causality measures applied to brain networks. J. Neurosci. Methods 215, 170–189. http://dx.doi.org/10.1016/j.jneumeth.2013.02.021.

Friston, K.J., 1994. Functional and effective connectivity in neuroimaging: a synthesis. Hum. Brain Mapp. 2, 56–78. http://dx.doi.org/10.1002/hbm.460020107.

Fuchs, M., Wagner, M., Kastner, J., 2007. Development of volume conductor and source models to localize epileptic foci. J. Clin. Neurophysiol. 24, 101–119. http://dx.doi.org/10.1097/WNP.0b013e318038fb3e.

Granger, C.W.J., 1969. Investigating causal relations by econometric models and cross-spectral methods. Econometrica 37, 424–438. http://dx.doi.org/10.2307/1912791.

Güllmar, D., Haueisen, J., Reichenbach, J.R., 2010. Influence of anisotropic electrical conductivity in white matter tissue on the EEG/MEG forward and inverse solution. A high-resolution whole head simulation study. NeuroImage 51, 145–163. http://dx.doi.org/10.1016/j.neuroimage.2010.02.014.

Hallez, H., Vanrumste, B., Van Hese, P., D'Asseler, Y., Lemahieu, I., Van de Walle, R., 2005. A finite difference method with reciprocity used to incorporate anisotropy in electroencephalogram dipole source localization. Phys. Med. Biol. 50, 3787. http://dx.doi.org/10.1088/0031-9155/50/16/009.

Hallez, H., Vanrumste, B., Van Hese, P., Delputte, S., Lemahieu, I., 2008. Dipole estimation errors due to differences in modeling anisotropic conductivities in realistic head models for EEG source analysis. Phys. Med. Biol. 53, 1877. http://dx.doi.org/10.1088/0031-9155/53/7/005.

Hämäläinen, M.S., Ilmoniemi, R.J., 1984. Interpreting measured magnetic fields of the brain: estimates of current distributions. Technical Report TKK-F-A599.

Hämäläinen, M.S., Ilmoniemi, R.J., 1994. Interpreting magnetic fields of the brain: minimum norm estimates. Med. Biol. Eng. Comput. 32, 35–42. http://dx.doi.org/10.1007/BF02512476.

Hämäläinen, M.S., Hari, R., Ilmoniemi, R.J., Knuutila, J., Lounasmaa, O., 1993. Magnetoencephalography — theory, instrumentation, and applications to noninvasive studies

of the working human brain. Rev. Mod. Phys. 65. http://dx.doi.org/10.1103/RevModPhys.65.413.
Haueisen, J., Ramon, C., Eiselt, M., Brauer, H., Nowak, H., 1997. Influence of tissue resistivities on neuromagnetic fields and electric potentials studied with a finite element model of the head. IEEE Trans. Biomed. Eng. 44, 727–735. http://dx.doi.org/10.1109/10.605429.
Haueisen, J., Tuch, D.S., Ramon, C., Schimpf, P.H., Wedeen, V.J., George, J.S., Belliveau, J.W., 2002. The influence of brain tissue anisotropy on human EEG and MEG. NeuroImage 15, 159–166. http://dx.doi.org/10.1006/nimg.2001.0962.
Haufe, S., Nikulin, V.V., Müller, K.-R., Nolte, G., 2013. A critical assessment of connectivity measures for EEG data: a simulation study. NeuroImage 64, 120–133. http://dx.doi.org/10.1016/j.neuroimage.2012.09.036.
He, B., Yang, L., Wilke, C., Yuan, H., 2011. Electrophysiological imaging of brain activity and connectivity—challenges and opportunities. IEEE Trans. Biomed. Eng. 58, 1918–1931. http://dx.doi.org/10.1109/TBME.2011.2139210.
Hillebrand, A., Barnes, G.R., Bosboom, J.L., Berendse, H.W., Stam, C.J., 2012. Frequency-dependent functional connectivity within resting-state networks: an atlas-based MEG beamformer solution. NeuroImage 59, 3909–3921. http://dx.doi.org/10.1016/j.neuroimage.2011.11.005.
Hipp, J.F., Engel, A.K., Siegel, M., 2011. Oscillatory synchronization in large-scale cortical networks predicts perception. Neuron 69, 387–396. http://dx.doi.org/10.1016/j.neuron.2010.12.027.
Hipp, J.F., Hawellek, D.J., Corbetta, M., Siegel, M., Engel, A.K., 2012. Large-scale cortical correlation structure of spontaneous oscillatory activity. Nat. Neurosci. 15, 884–890. http://dx.doi.org/10.1038/nn.3101.
Horwitz, B., 2003. The elusive concept of brain connectivity. NeuroImage 19, 466–470. http://dx.doi.org/10.1016/S1053-8119(03)00112-5.
Huang, M.-X., Song, T., Hagler, J., Donald, J., Podgorny, I., Jousmaki, V., Cui, L., Gaa, K., Harrington, D.L., Dale, A.M., Lee, R.R., Elman, J., Halgren, E., 2007. A novel integrated MEG and EEG analysis method for dipolar sources. NeuroImage 37, 731–748. http://dx.doi.org/10.1016/j.neuroimage.2007.06.002.
Hui, H.B., Pantazis, D., Bressler, S.L., Leahy, R.M., 2010. Identifying true cortical interactions in MEG using the nulling beamformer. NeuroImage 49, 3161–3174. http://dx.doi.org/10.1016/j.neuroimage.2009.10.078.
Hyde, D.E., Duffy, F.H., Warfield, S.K., 2012. Anisotropic partial volume CSF modeling for EEG source localization. NeuroImage 62, 2161–2170. http://dx.doi.org/10.1016/j.neuroimage.2012.05.055.
Jansen, B.H., Rit, V.G., 1995. Electroencephalogram and visual evoked potential generation in a mathematical model of coupled cortical columns. Biol. Cybern. 73, 357–366. http://dx.doi.org/10.1007/BF00199471.
Kaipio, J., Somersalo, E., 2007. Statistical inverse problems: discretization, model reduction and inverse crimes. J. Comput. Appl. Math. 198, 493–504. http://dx.doi.org/10.1016/j.cam.2005.09.027.
Kamiński, M.J., Blinowska, K.J., 1991. A new method of the description of the information flow in the brain structures. Biol. Cybern. 65, 203–210. http://dx.doi.org/10.1007/BF00198091.
Kamiński, M., Liang, H., 2005. Causal influence: advances in neurosignal analysis. Crit. Rev. Biomed. Eng. 33, 347–430. http://dx.doi.org/10.1615/CritRevBiomedEng.v33.i4.20.
Kiebel, S.J., David, O., Friston, K.J., 2006. Dynamic causal modelling of evoked responses in EEG/MEG with lead field parameterization. NeuroImage 30, 1273–1284. http://dx.doi.org/10.1016/j.neuroimage.2005.12.055.
Kujala, J., Pammer, K., Cornelissen, P., Roebroeck, A., Formisano, E., Salmelin, R., 2007. Phase coupling in a cerebro-cerebellar network at 8–13 Hz during reading. Cereb. Cortex 17, 1476–1485. http://dx.doi.org/10.1093/cercor/bhl059.
Kus, R., Kaminski, M., Blinowska, K.J., 2004. Determination of EEG activity propagation: pair-wise versus multichannel estimate. IEEE Trans. Biomed. Eng. 51, 1501–1510. http://dx.doi.org/10.1109/TBME.2004.827929.
Kybic, J., Clerc, M., Abboud, T., Faugeras, O., Keriven, R., Papadopoulo, T., 2005. A common formalism for the integral formulations of the forward EEG problem. IEEE Trans. Med. Imaging 24, 12–28. http://dx.doi.org/10.1109/TMI.2004.837363.
Lachaux, J.P., Rodriguez, E., Martinerie, J., Varela, F.J., 1999. Measuring phase synchrony in brain signals. Hum. Brain Mapp. 8, 194–208. http://dx.doi.org/10.1002/(SICI)1097-0193(1999)8:4<194::AID-HBM4>3.0.CO;2-C.
Lanfer, B., Paul-Jordanov, I., Scherg, M., Wolters, C.H., 2012a. Influence of interior cerebrospinal fluid compartments on EEG source analysis. Biomed. Tech. (Berl.) 57, 623–626. http://dx.doi.org/10.1515/bmt-2012-4020.
Lanfer, B., Scherg, M., Dannhauer, M., Knösche, T.R., Burger, M., Wolters, C.H., 2012b. Influences of skull segmentation inaccuracies on EEG source analysis. NeuroImage 62, 418–431. http://dx.doi.org/10.1016/j.neuroimage.2012.05.006.
Lanfer, B., Röer, C., Scherg, M., Rampp, S., Kellinghaus, C., Wolters, C.H., 2013. Influence of a silastic ECoG grid on EEG/ECoG based source analysis. Brain Topogr. 26, 212–228. http://dx.doi.org/10.1007/s10548-012-0251-0.
Lew, S., Wolters, C.H., Anwander, A., Makeig, S., Macleod, R.S., 2009a. Improved EEG source analysis using low-resolution conductivity estimation in a four-compartment finite element head model. Hum. Brain Mapp. 30, 2862–2878. http://dx.doi.org/10.1002/hbm.20714.
Lew, S., Wolters, C.H., Dierkes, T., Röer, C., Macleod, R.S., 2009b. Accuracy and run-time comparison for different potential approaches and iterative solvers in finite element method based EEG source analysis. Appl. Numer. Math. 59, 1970–1988. http://dx.doi.org/10.1016/j.apnum.2009.02.006.
Lew, S., Sliva, D.D., Choe, M.-s., Grant, P.E., Okada, Y., Wolters, C.H., Hämäläinen, M.S., 2013. Effects of sutures and fontanels on MEG and EEG source analysis in a realistic infant head model. NeuroImage 76, 282–293. http://dx.doi.org/10.1016/j.neuroimage.2013.03.017.
Lu, Y., Yang, L., Worrell, G.a., He, B., 2012. Seizure source imaging by means of FINE spatio-temporal dipole localization and directed transfer function in partial epilepsy patients. Clin. Neurophysiol. 123, 1275–1283. http://dx.doi.org/10.1016/j.clinph.2011.11.007.
Marin, G., Guerin, C., Baillet, S., Garnero, L., Meunier, G., 1998. Influence of skull anisotropy for the forward and inverse problem in EEG: simulation studies using FEM on realistic head models. Hum. Brain Mapp. 6, 250–269. http://dx.doi.org/10.1002/(SICI)1097-0193(1998)6:4<250::AID-HBM5>3.0.CO;2-2.
Martino, J., Honma, S.M., Findlay, A.M., Guggisberg, A.G., Owen, J.P., Kirsch, H.E., Berger, M.S., Nagarajan, S.S., 2011. Resting functional connectivity in patients with brain tumors in eloquent areas. Ann. Neurol. 69, 521–532. http://dx.doi.org/10.1002/ana.22167.
Meijs, J.W.h., Weier, O.W., Peters, M.J., Van, O.A., 1989. On the numerical accuracy of the boundary element method. IEEE Trans. Biomed. Eng. 36, 1038–1049. http://dx.doi.org/10.1109/10.40805.
Montes-Restrepo, V., van Mierlo, P., Strobbe, G., Staelens, S., Vandenberghe, S., Hallez, H., 2014. Influence of skull modeling approaches on EEG source localization. Brain Topogr. 27, 95–111. http://dx.doi.org/10.1007/s10548-013-0313-y.
Nolte, G., Bai, O., Wheaton, L., Mari, Z., Vorbach, S., Hallett, M., 2004. Identifying true brain interaction from EEG data using the imaginary part of coherency. Clin. Neurophysiol. 115, 2292–2307. http://dx.doi.org/10.1016/j.clinph.2004.04.029.
Oostenveld, R., Oostendorp, T.F., 2002. Validating the boundary element method for forward and inverse EEG computations in the presence of a hole in the skull. Hum. Brain Mapp. 17, 179–192. http://dx.doi.org/10.1002/hbm.10061.
Palva, S., Palva, J.M., 2012. Discovering oscillatory interaction networks with M/EEG: challenges and breakthroughs. Trends Cogn. Sci. 16, 219–230. http://dx.doi.org/10.1016/j.tics.2012.02.004.
Palva, J.M., Monto, S., Kulashekhar, S., Palva, S., 2010. Neuronal synchrony reveals working memory networks and predicts individual memory capacity. Proc. Natl. Acad. Sci. U. S. A. 107, 7580–7585. http://dx.doi.org/10.1073/pnas.0913113107.
Ramon, C., Schimpf, P., Haueisen, J., Holmes, M., Ishimaru, A., 2004. Role of soft bone, CSF and gray matter in EEG simulations. Brain Topogr. 16, 245–248. http://dx.doi.org/10.1023/B:BRAT.0000032859.68959.76.
Rappelsberger, P., Petsche, H., 1988. Probability mapping: power and coherence analyses of cognitive processes. Brain Topogr. 1, 46–54. http://dx.doi.org/10.1007/BF01129339.
Rice, J.K., Rorden, C., Little, J.S., Parra, L.C., 2013. Subject position affects EEG magnitudes. NeuroImage 64, 476–484. http://dx.doi.org/10.1016/j.neuroimage.2012.09.041.
Rullmann, M., Anwander, A., Dannhauer, M., Warfield, S.K., Duffy, F.H., Wolters, C.H., 2009. EEG source analysis of epileptiform activity using a 1 mm anisotropic hexahedra finite element head model. NeuroImage 44, 399. http://dx.doi.org/10.1016/j.neuroimage.2008.09.009.
Sadleir, R.J., Argibay, A., 2007. Modeling skull electrical properties. Ann. Biomed. Eng. 35, 1699–1712. http://dx.doi.org/10.1007/s10439-007-9343-5.
Schimpf, P.H., Ramon, C., Haueisen, J., 2002. Dipole models for the EEG and MEG. IEEE Trans. Biomed. Eng. 49, 409–418. http://dx.doi.org/10.1109/10.995679.
Schlögl, A., 2006. A comparison of multivariate autoregressive estimators. Signal Process. 86, 2426–2429. http://dx.doi.org/10.1016/j.sigpro.2005.11.007.
Schneider, T., Neumaier, A., 2001. Algorithm 808: ARfit-A Matlab package for the estimation of parameters and eigenmodes of multivariate autoregressive models. ACM Trans. Math. Softw. 27, 58–65. http://dx.doi.org/10.1145/382043.382316.
Schnitzler, A., Gross, J., 2005. Normal and pathological oscillatory communication in the brain. Nat. Rev. Neurosci. 6, 285–296. http://dx.doi.org/10.1038/nrn1650.
Schoffelen, J.-M., Gross, J., 2009. Source connectivity analysis with MEG and EEG. Hum. Brain Mapp. 30, 1857–1865. http://dx.doi.org/10.1002/hbm.20745.
SCIRun, 2014. SCIRun: A Scientific Computing Problem Solving Environment. Scientific Computing and Imaging Institute (SCI) (http://www.scirun.org).
Sekihara, K., Nagarajan, S.S., 2008. Adaptive Spatial Filters for Electromagnetic Brain Imaging. Springer http://dx.doi.org/10.1007/978-3-540-79370-0.
Sekihara, K., Nagarajan, S.S., Poeppel, D., Marantz, A., 2004. Asymptotic SNR of scalar and vector minimum-variance beamformers for neuromagnetic source reconstruction. IEEE Trans. Biomed. Eng. 51, 1726–1734. http://dx.doi.org/10.1109/TBME.2004.827926.
Sekihara, K., Sahani, M., Nagarajan, S.S., 2005. Localization bias and spatial resolution of adaptive and non-adaptive spatial filters for MEG source reconstruction. NeuroImage 25, 1056–1067. http://dx.doi.org/10.1016/j.neuroimage.2004.11.051.
Sekihara, K., Owen, J.P., Trisno, S., Nagarajan, S.S., 2011. Removal of spurious coherence in MEG source-space coherence analysis. IEEE Trans. Biomed. Eng. 58, 3121–3129. http://dx.doi.org/10.1109/TBME.2011.2162514.
Shim, M., Kim, D.-W., Lee, S.-H., Im, C.-H., 2014. Disruptions in small-world cortical functional connectivity network during an auditory oddball paradigm task in patients with schizophrenia. Schizophr. Res. 156, 197–203. http://dx.doi.org/10.1016/j.schres.2014.04.012.
SimBio, 2014. SimBio: A Generic Environment for Bio-numerical Simulation. https://www.mrt.uni-jena.de/neurofem/index.php/Main_Page.
Smith, S.M., Jenkinson, M., Woolrich, M.W., Beckmann, C.F., Behrens, T.E.J., Johansen-Berg, H., Bannister, P.R., De Luca, M., Drobnjak, I., Flitney, D.E., Niazy, R.K., Saunders, J., Vickers, J., Zhang, Y., De Stefano, N., Brady, J.M., Matthews, P.M., 2004. Advances in functional and structural MR image analysis and implementation as FSL. NeuroImage 23 (Suppl. 1), S208–S219. http://dx.doi.org/10.1016/j.neuroimage.2004.07.051.
Spiegler, A., Kiebel, S.J., Atay, F.M., Knösche, T.R., 2010. Bifurcation analysis of neural mass models: impact of extrinsic inputs and dendritic time constants. NeuroImage 52, 1041–1058. http://dx.doi.org/10.1016/j.neuroimage.2009.12.081.
Steinsträter, O., Sillekens, S., Junghoefer, M., Burger, M., Wolters, C.H., 2010. Sensitivity of beamformer source analysis to deficiencies in forward modeling. Hum. Brain Mapp. 31, 1907–1927. http://dx.doi.org/10.1002/hbm.20986.
Stenroos, M., Hunold, A., Haueisen, J., 2014. Comparison of three-shell and simplified volume conductor models in magnetoencephalography. NeuroImage 94, 337–348. http://dx.doi.org/10.1016/j.neuroimage.2014.01.006.

Taubin, G., 1995. A signal processing approach to fair surface design. Proceedings of the 22nd annual conference on Computer graphics and interactive techniques. ACM, pp. 351–358 http://dx.doi.org/10.1145/218380.218473.
Tetgen, 2014. TetGen: A Quality Tetrahedral Mesh Generator and a 3D Delaunay Triangulator. http://www.tetgen.org.
van den Broek, S.P., Reinders, F., Donderwinkel, M., Peters, M.J., 1998. Volume conduction effects in EEG and MEG. Electroencephalogr. Clin. Neurophysiol. 106, 522–534. http://dx.doi.org/10.1016/S0013-4694(97)00147-8.
Van Uitert, R., Weinstein, D., Johnson, C., 2003. Volume currents in forward and inverse magnetoencephalographic simulations using realistic head models. Ann. Biomed. Eng. 31, 21–31. http://dx.doi.org/10.1114/1.1535412.
Van Veen, B.D., van Drongelen, W., Yuchtman, M., Suzuki, A., 1997. Localization of brain electrical activity via linearly constrained minimum variance spatial filtering. IEEE Trans. Biomed. Eng. 44, 867–880. http://dx.doi.org/10.1109/10.623056.
Vanrumste, B., Van Hoey, G., Van de Walle, R., D'Havé, M., Lemahieu, I., Boon, P., 2000. Dipole location errors in electroencephalogram source analysis due to volume conductor model errors. Med. Biol. Eng. Comput. 38, 528–534. http://dx.doi.org/10.1007/BF02345748.
Varela, F., Lachaux, J.-P., Rodriguez, E., Martinerie, J., 2001. The brainweb: phase synchronization and large-scale integration. Nat. Rev. Neurosci. 2, 229–239. http://dx.doi.org/10.1038/35067550.
Vese, L.A., Chan, T.F., 2002. A multiphase level set framework for image segmentation using the Mumford and Shah model. Int. J. Comput. Vis. 50, 271–293. http://dx.doi.org/10.1023/A:1020874308076.
Vorwerk, J., 2011. Comparison of Numerical Approaches to the EEG Forward Problem. Westfälische Wilhelms-Universität Münster (http://wwwmath.uni-muenster.de/num/Arbeitsgruppen/ag_burger/organization/burger/pictures/DA%20Vorwerk.pdf).
Vorwerk, J., Clerc, M., Burger, M., Wolters, C.H., 2012. Comparison of boundary element and finite element approaches to the EEG forward problem. Biomed. Tech. (Berl.) 57, 795–798. http://dx.doi.org/10.1515/bmt-2012-4152.
Vorwerk, J., Cho, J.-H., Rampp, S., Hamer, H., Knösche, T.R., Wolters, C.H., 2014. A guideline for head volume conductor modeling in EEG and MEG. NeuroImage 100, 590–607. http://dx.doi.org/10.1016/j.neuroimage.2014.06.040.
Vrba, J., Robinson, S.E., 2001. Signal processing in magnetoencephalography. Methods 25, 249–271. http://dx.doi.org/10.1006/meth.2001.1238.
Wibral, M., Rahm, B., Rieder, M., Lindner, M., Vicente, R., Kaiser, J., 2011. Transfer entropy in magnetoencephalographic data: quantifying information flow in cortical and cerebellar networks. Prog. Biophys. Mol. Biol. 105, 80–97. http://dx.doi.org/10.1016/j.pbiomolbio.2010.11.006.
Wolters, C.H., Grasedyck, L., Hackbusch, W., 2004. Efficient computation of lead field bases and influence matrix for the FEM-based EEG and MEG inverse problem. Inverse Probl. 20, 1099–1116. http://dx.doi.org/10.1088/0266-5611/20/4/007.
Wolters, C.H., Anwander, A., Tricoche, X., Weinstein, D., Koch, M.A., Macleod, R.S., 2006. Influence of tissue conductivity anisotropy on EEG/MEG field and return current computation in a realistic head model: a simulation and visualization study using high-resolution finite element modeling. NeuroImage 30, 813–826. http://dx.doi.org/10.1016/j.neuroimage.2005.10.014.